

# Patterns of valley incision beneath the Greenland Ice Sheet revealed using automated mapping and classification

Guy J.G. Paxman\*

Department of Geography, Durham University, South Road, Durham DH1 3LE, UK

## ARTICLE INFO

### Keywords:

Greenland Ice Sheet  
Radioglaciology  
Machine learning  
Subglacial topography  
Valley incision  
Landscape evolution

## ABSTRACT

The Greenland Ice Sheet covers an area of 1.7 million km<sup>2</sup>, equivalent to ~79 % of the surface of Kalaallit Nunaat (Greenland) and ~1.2 % of the Earth's land surface. The macro-scale geomorphology beneath the ice can provide a valuable record of past ice sheet behaviour, particularly during warm periods that may serve as analogues for present and future climates. However, despite extensive mapping of the landscape by airborne radar surveying, Greenland's subglacial geomorphology remains comparatively understudied. Here we construct an automated workflow to identify, extract, and quantify the morphology of valley cross-sectional profiles across Greenland, as observed in NASA Operation IceBridge radar data. We identify 5335 cross-sectional profiles and apply a supervised machine learning method to classify valleys based on their morphological similarity to those formed by glacial or fluvial incision elsewhere in the Northern Hemisphere. Approximately two thirds of the valleys are classified as 'glacial', some of which reflect active incision at the modern ice sheet margin, whereas others are situated beneath cold-based, slow-moving ice, indicating that they were incised under a different ice configuration earlier in Greenland's glacial history. The presence of 'fluvial' valleys in the low-lying interior of northern Greenland and in mountainous southern Greenland suggests parts of the inherited landscape formed under ice-free conditions during pre- or inter-glacial times have been preserved due to negligible long-term subglacial erosion rates. Some low-lying catchments show hallmarks of a combination of fluvial, glacial, and glacio-fluvial incision, hinting at complex interplays between valley-forming processes over the history of the Greenland Ice Sheet.

## 1. Introduction

The Greenland Ice Sheet (GrIS; Fig. 1a) contains approximately three million cubic kilometres of ice, which is equivalent to ~7.4 m of global sea level change (Morlighem et al., 2017). Today, ice loss from the GrIS, driven by rising atmosphere and ocean temperatures caused by anthropogenic activity, is one of the largest contributors to global sea level rise (Cazenave et al., 2018). Mass balance calculations indicate that between 1992 and 2018 the GrIS lost mass at an average rate of ~140 Gt year<sup>-1</sup>, which is equivalent to a global mean sea level contribution of ~1.1 cm over this period (The Imbie Team, 2020). This mass loss has been driven by approximately equal contributions from increased surface melting and enhanced discharge from outlet glaciers (The Imbie Team, 2020).

Ice sheet model ensemble experiments indicate that without a substantial reduction in global greenhouse gas emissions, rates of ice mass loss in Greenland are likely to accelerate over the course of the current

century (Goelzer et al., 2020). However, recent studies continue to show a broad range of projected GrIS contributions to sea level rise by 2100 CE, including (for the high emissions RCP 8.5/SSP5-85 scenario) 9 ± 5 cm (Goelzer et al., 2020), 10 ± 8 cm (Edwards et al., 2021), and 19 ± 10 cm (Aschwanden and Brinkerhoff, 2022). These ranges reflect the intrinsic uncertainties in the ice models, climate models, and ocean forcing (Goelzer et al., 2020), as well as gaps in our understanding of physical processes including ice-atmosphere, ice-Earth, and ice-ocean interactions (Edwards et al., 2019; Noble et al., 2020; Straneo and Heimbach, 2013; Whitehouse et al., 2019). Reducing these uncertainties in future sea level projections is of especial importance for assessing global societal impacts and establishing successful mitigation and adaptation strategies.

Uncertainties in projections of future ice sheet and sea level change can be reduced by improving our understanding of the past behaviour of the GrIS (e.g., during warmer climate intervals), which can be constrained using geological records (e.g., Alley et al., 2010; Bierman et al.,

\* Corresponding author.

E-mail address: [guy.j.paxman@durham.ac.uk](mailto:guy.j.paxman@durham.ac.uk).

<https://doi.org/10.1016/j.geomorph.2023.108778>

Received 11 April 2023; Received in revised form 5 June 2023; Accepted 5 June 2023

Available online 9 June 2023

0169-555X/© 2023 The Author(s). Published by Elsevier B.V. This is an open access article under the CC BY license (<http://creativecommons.org/licenses/by/4.0/>).

2016). The (in)ability of ice sheet models to accurately reproduce these records of past behaviour can provide valuable constraints on model physics and parameter space, which in turn imparts increased confidence when using these models to simulate future change.

## 2. Motivation

### 2.1. Subglacial topography as a record of long-term ice behaviour

Based on records from offshore sedimentary material, intensification of widespread glaciation of Greenland is generally believed to have occurred during the late Pliocene to early Pleistocene (ca. 3.6–2.4 Ma) (Flesche Kleiven et al., 2002; Jansen et al., 2000; Mudelsee and Raymo, 2005). However, many uncertainties persist regarding the history of the GrIS prior to, during, and following this interval (e.g., Bierman et al., 2016; DeConto et al., 2008; Eldrett et al., 2007; Schaefer et al., 2016; Tripathi and Darby, 2018). Building an improved understanding of GrIS behaviour during its early development and through subsequent warm

periods will provide valuable analogues for predicting its response to current and projected future atmosphere and ocean warming. Constraining the stability, extent, and dynamics of past ice sheets in Greenland will also help (i) improve cryospheric boundary conditions in palaeoclimate and ocean modelling (Haywood et al., 2019), (ii) deconvolve marine records of past global ice volume, temperature, and sea level (Miller et al., 2020), and (iii) reduce the variance in numerical model simulations of past GrIS behaviour, and in turn increase confidence in applying such models to predict future glaciological change (Goelzer et al., 2020).

However, acquiring further data-based constraints of palaeo-ice extent and dynamics during times of more restricted ice cover is challenging given that onshore records pertaining to these intervals are largely obscured by the modern-day GrIS. Elsewhere in the northern hemisphere, an important tool for constraining the extent and behaviour of former ice sheets is mapping their geomorphological imprint upon the landscape (e.g., Bickerdike et al., 2018; Boulton and Clark, 1990; Clark et al., 2022; Kleman et al., 1997; Margold et al., 2013). By contrast,

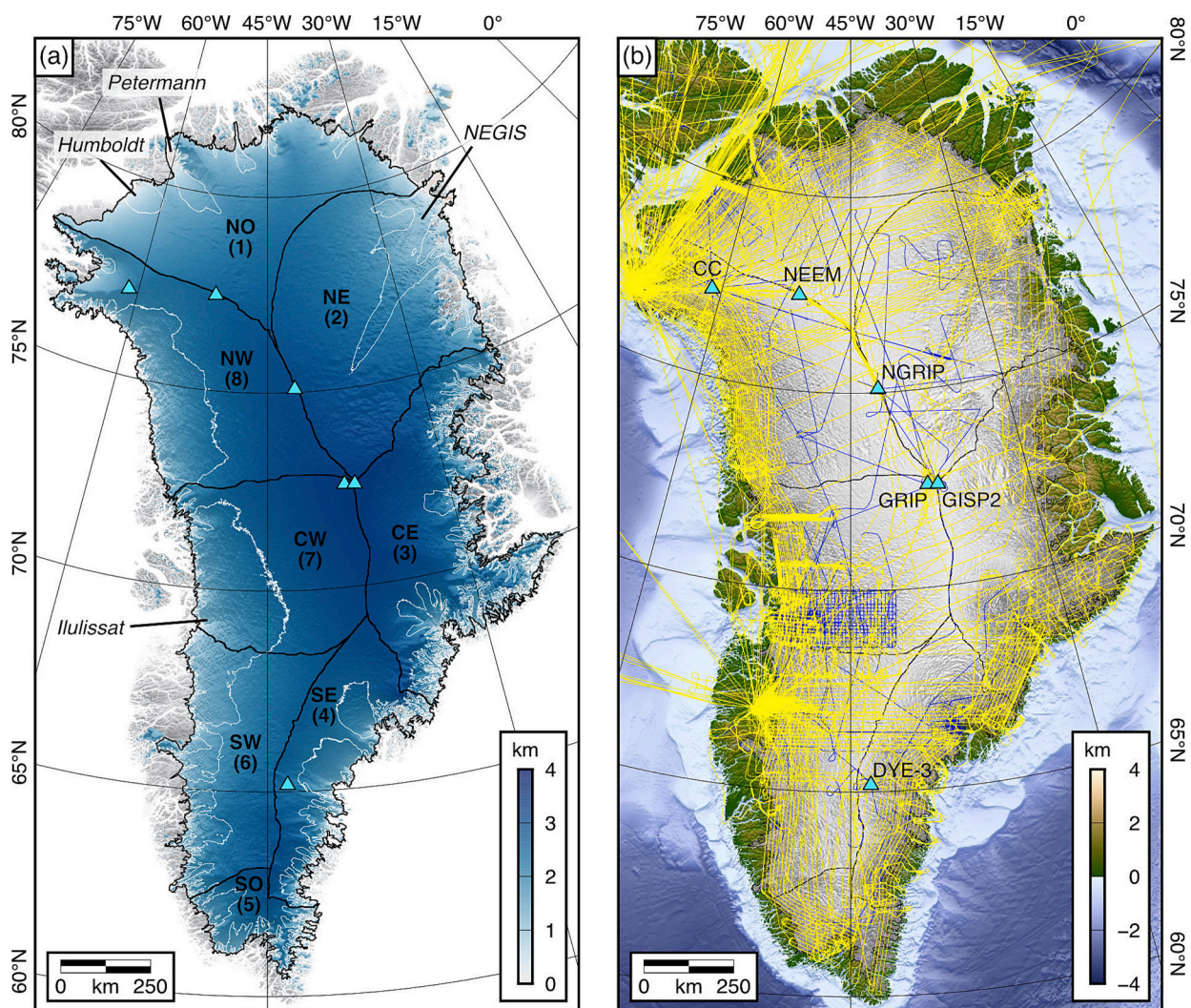


**Fig. 1.** Greenland Ice Sheet configuration and airborne radar data coverage. (a) Surface elevation of the Greenland Ice Sheet (Howat et al., 2022, 2014). Black outlines delineate the ice margin and eight first-order drainage catchments (Zwally et al., 2012). Catchment abbreviations: NO = north; NE = northeast; CE = central east; SE = southeast; SO = south; SW = southwest; CW = central west; NW = northwest. Land elevation outside the ice sheet margin (Morlighem et al., 2017) is shaded in greyscale. The 50 m/yr ice surface velocity contour (Joughin et al., 2018), an approximate threshold of the onset of fast flow, is marked by the white outline. Labels mark outlet glaciers referenced in the main text. (b) Coverage of radio-echo sounding (radar) data used in this study. Hillshade image of the ice surface elevation model (Howat et al., 2022, 2014) is shaded in greyscale; land surface topography and sea floor bathymetry (Morlighem et al., 2017) are displayed according to the colour scale. All elevations are relative to global mean sea level. Blue triangles mark deep ice core sites. RES survey lines used in this study: yellow = OIB survey flights (2010–2019), blue = legacy CReSIS flights (2000–2009) (Paden et al., 2019).

analysis of Greenland's subglacial geomorphology has historically been limited by a lack of direct measurements of the ice sheet bed. However, in the past two decades the bed topography of Greenland has been extensively mapped using radio-echo sounding (RES) surveying, including >800,000 line-km of data acquired during NASA's Operation IceBridge (OIB) mission between 2010 and 2019 (Fig. 1b) (MacGregor et al., 2021). Although RES-derived bed elevation data have been analysed in certain regions (e.g., Cooper et al., 2016; Livingstone et al., 2017; MacGregor et al., 2019), significant amounts of data remain under-utilised and systematic island-wide analyses of the subglacial landscape have been lacking.

## 2.2. Study objectives

In this study, we seek to make use of the full OIB RES dataset to carry out a systematic continental-scale analysis of geomorphological features within Greenland's subglacial landscape. Specifically, we use OIB MCoRDS (Multi-Channel Coherent Radar Depth Sounder) Level 2 pre-processed ice thickness and bed elevation measurements (Paden et al., 2019), together with legacy CReSIS (Center for Remote Sensing and Integrated Systems) survey data collected between 2000 and 2009 (Fig. 1b). Given the size and extent of this dataset, which contains >30 million bed elevation datapoints along >800,000 line-km, a large-scale geomorphological analysis using traditional manual mapping techniques would be highly laborious. Instead, we aim to develop automated techniques to enable time-efficient mapping and classification of large numbers of macro-scale geomorphological features. Such methods have been employed in the classification of subaerial landforms (Allred and Luo, 2016; Brigham and Crider, 2022; Robb et al., 2015) and subglacial geological domains (Li et al., 2022), but have not been previously applied to the subglacial landscape of Greenland.

Here we focus specifically on subglacial valleys, which have been documented in multiple regions of Greenland (Bamber et al., 2013; Cooper et al., 2016; Dam et al., 2020; Livingstone et al., 2017; Paxman et al., 2021). The reasons for focussing on this particular type of landform are: (i) RES survey lines provide a cross-sectional (2D) view of topography; valleys are more readily discerned in cross-section than other landforms, (ii) valley cross-profile morphology can be used to differentiate between different styles of erosion (e.g., Harbor and Wheeler, 1992), and (iii) no unified framework currently exists for comparing patterns of valley extent and morphology across Greenland. As well as helping constrain the geological, erosional, and climatological history of a landscape (Cooper et al., 2016; Franke et al., 2021; Paxman et al., 2021), subglacial valleys can also exert a significant control on contemporary ice flow and stability (Cooper et al., 2016; Morlighem et al., 2017).

## 3. Methods

We developed an automated workflow to identify the locations of subglacial valleys across Greenland and quantify the morphometry of their cross-profiles. We then used supervised machine learning to classify subglacial valleys according to their morphological similarity with valleys observed elsewhere in the Northern Hemisphere that have, or have not, been extensively modified by Quaternary glacial erosion. An advantage of adopting a supervised machine learning approach is that it avoids the need to explicitly impose hard-to-define morphometric criteria to classify landforms (Jamieson et al., 2014; Livingstone et al., 2017), instead relying on statistical comparison with the 'training dataset', which contains valleys whose origin is well understood. Our overarching aim is to improve understanding of the distribution and evolution of valley networks across Greenland, and their implications for past and present ice dynamics. Our workflow can be divided into four principal steps.

### 3.1. Construction of the training dataset

The training dataset comprises 'labelled' valleys against which the 'unlabelled' Greenland valleys are compared and consequently assigned a class. It is therefore important that the training dataset captures the variability of the unlabelled valleys. Hence, we selected valleys with a well-understood mode of formation from regions with a close geological affinity to Greenland. This included passive margin settings in the Northern Hemisphere, such as northwest Europe, northwest Africa, and eastern North America, as well as regions with orogens that have experienced Cenozoic uplift, such as western North America and the European Alps. The training dataset therefore includes valleys from a range of geological and tectonic settings representative of those found in Greenland (Henriksen et al., 2009). Given that Greenland is not experiencing active tectonics, we avoided valleys from sites experiencing significant active continental deformation.

Valleys in the training dataset were labelled as either 'glacial' or 'fluvial' based on whether they possess a significant erosive imprint from Quaternary glaciation. Although achieving a comprehensive understanding of the spatiotemporal evolution of even a well-mapped subaerial landscape is challenging, valleys from the Scottish Highlands, Canadian Rockies, Norwegian Caledonides, and European Alps are known to have experienced extensive modification by Quaternary glacial incision (Fig. 2) (Hall et al., 2013; Hilley et al., 2020; Penck, 1905; Sugden, 1968), so were labelled as 'glacial'. By contrast, valleys from the Atlas Mountains (Morocco), Cumberland Plateau (Appalachian Mountains, USA), Sierra Nevada (California, USA; only valleys below the mapped LGM glacial limit (Gillespie and Clark, 2011)), and Sierra Nevada (Spain) are recognised as being unmodified by glacial incision and retaining a primarily fluvial signature (Fig. 3) (Egholm et al., 2009; Stokes et al., 2008; Sugden, 1977; Zimmer and Gabet, 2018), so were labelled as 'fluvial'. Cross-profiles were sampled orthogonal to the trend of the valleys at randomly selected points, and were extracted from the Copernicus 90 m global digital elevation model (DEM) (European Space Agency, 2021).

Although there is no definitive 'correct' size for the training dataset, a common rule-of-thumb is that the number of entries in the training dataset should be at least 10 times the number of independent variables that define each entry, and conservatively at least 50 times this number (Alwosheel et al., 2018). In this study, each valley is defined by 4 morphometric variables (see Section 3.2), so we selected 200 valleys to comprise the training dataset: 100 from the four 'glacial' regions and 100 from the four 'fluvial' regions.

### 3.2. Calculation of valley morphometric indices

Fluvial and glacial erosion are associated with different diagnostic valley cross-profiles. For example, flow of glacial ice and associated erosion often leads to widening and deepening of a valley and the formation of characteristic 'U-shaped' or parabolic cross-profiles, as opposed to the more linear slopes of a 'V-shaped' fluvial valley (Brook et al., 2006; Davila et al., 2013; Harbor and Wheeler, 1992). For each cross-profile ( $z(x)$ ) in the training dataset, we extracted four quantitative metrics that characterise valley morphology (Fig. 4).

(i) valley depth (D), defined as the average difference in elevation between the two valley rims ( $Z_{R1}$  and  $Z_{R2}$ ) and the valley bottom ( $Z_B$ ) (Fig. 4a)

$$D = \frac{Z_{R1} + Z_{R2}}{2} - Z_B. \quad (1)$$

(ii) valley top (ridge-to-ridge) width ( $W_{top}$ ), defined as the horizontal distance between the two valley rims ( $X_{R1}$  and  $X_{R2}$ ) (Fig. 4c)

$$W_{top} = |X_{R2} - X_{R1}|. \quad (2)$$

(iii) the V-index (V), which is defined as the ratio between the valley cross-sectional area ( $A_x$ ) and the area of an idealised V-shaped valley

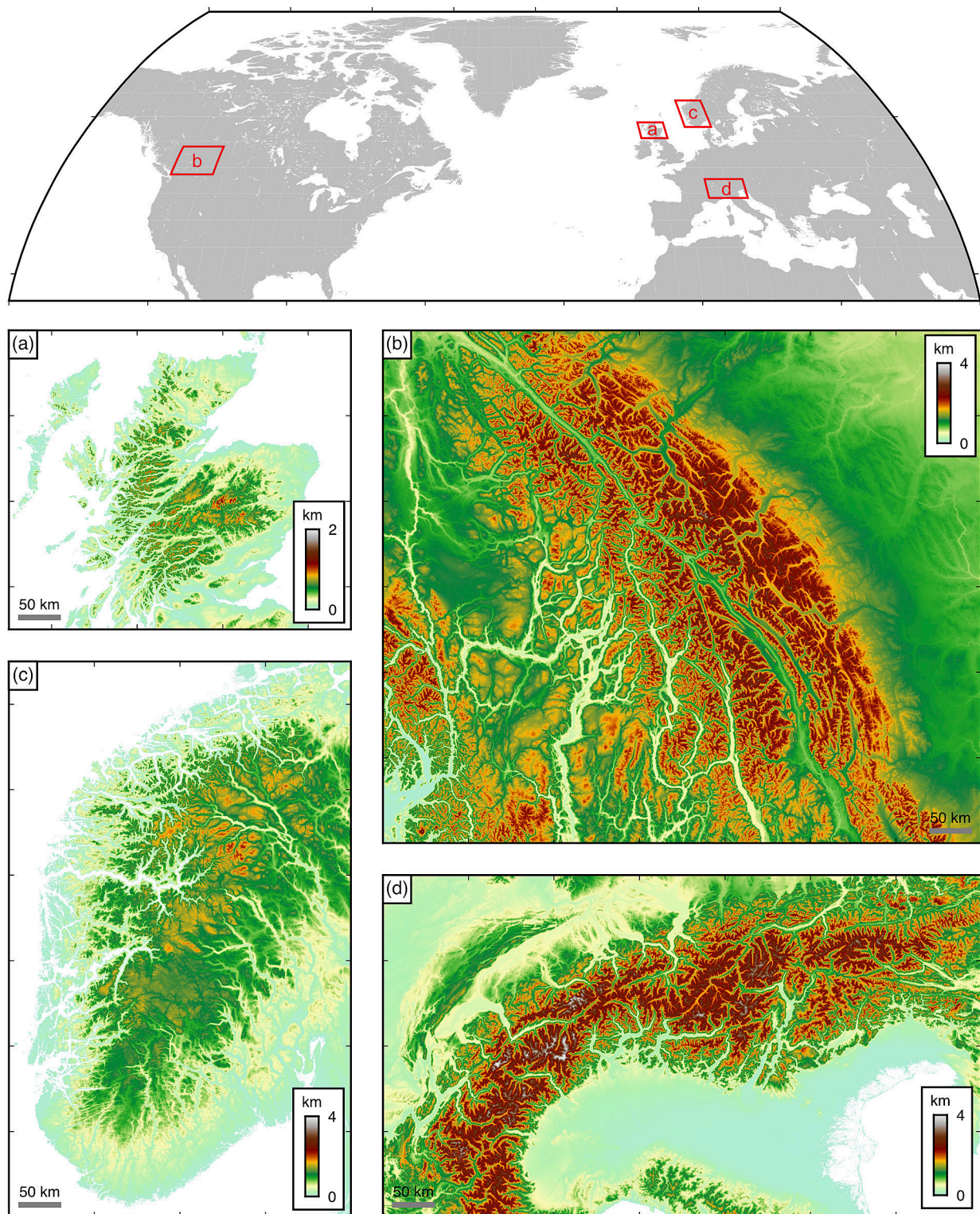


**Fig. 2.** Locations of glacial valley training data. These regions contain valleys that have experienced significant modification by Quaternary glaciation. Elevations are taken from the Copernicus 90 m global digital elevation model (European Space Agency, 2021). (a) Scottish Highlands, (b) Canadian Rockies, (c) Norwegian Caledonides, (d) European Alps. Note that the elevation scale in panel a differs from the other panels. Top: map shows the locations of the four panels.

with the same rim and floor co-ordinates ( $A_v$ ) (Zimmer and Gabet, 2018)

$$V = \frac{A_x}{A_v} - 1. \quad (3)$$

For an idealised V-shaped valley,  $A_x$  will be equal to  $A_v$ , and the V-index will be equal to zero. For valleys that are increasingly U-shaped,

the area of the cross-section will increase, such that the ratio defined in Eq. (3) will increase above zero. To avoid an influence from low-angle and/or convex slopes near the rims of the valley, which may not have been subject to glacial erosion (Zimmer and Gabet, 2018), the V-index is calculated for a truncated section of the cross profile below 80 % of the full relief on each side of the valley (Fig. 4e).

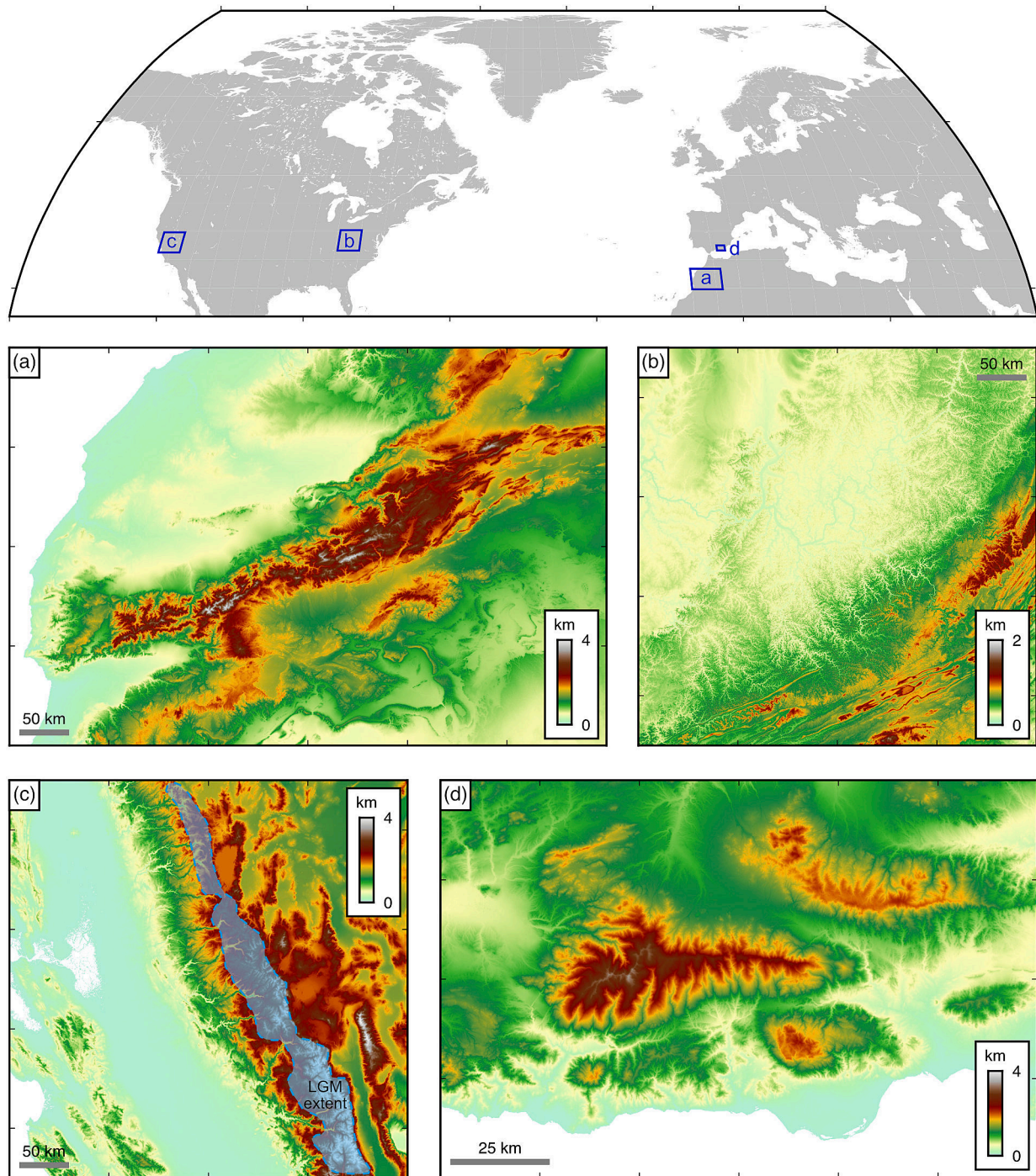


**Fig. 3.** Locations of fluvial valley training data. These regions contain valleys that have not experienced significant modification by Quaternary glaciation. Elevations are taken from the Copernicus 90 m global digital elevation model (European Space Agency, 2021). (a) Atlas Mountains, (b) Cumberland Plateau (Appalachians), (c) Sierra Nevada, California (only valleys outside of the labelled LGM glacial limit (Gillespie and Clark, 2011)), (d) Sierra Nevada, Spain. Note that the elevation scale in panel b differs from the other panels. Top: map shows the locations of the four panels.

(iv) the ratio ( $C$ ) between the curvature (second spatial derivative) of two second-order polynomials: one fitted to the central 20 % of the valley cross-sectional profile ( $\kappa_{20}$ ) and the second to the central 80 % of the valley cross-sectional profile ( $\kappa_{80}$ ).

$$C = 1 - \frac{\kappa_{20}}{\kappa_{80}} \quad (4)$$

For an idealised V-shaped valley, the concavity of the inner (20 %) sub-section will be approximately equal to that of the outer (80 %) sub-section. For valleys that are increasingly U-shaped, the concavity of the

inner sub-section will be lower than that of the outer sub-section, such that the ratio defined in Eq. (4) will increase above zero. The inner sub-section was defined as the section of the cross-profile below 20 % of the total relief and the outer sub-section as the section of the cross-profile below 80 % of the total relief (Fig. 4g).

The second-order polynomial that best fits a valley profile in the least-squares sense is given as

$$f(x) = ax^2 + bx + c, \quad (5)$$

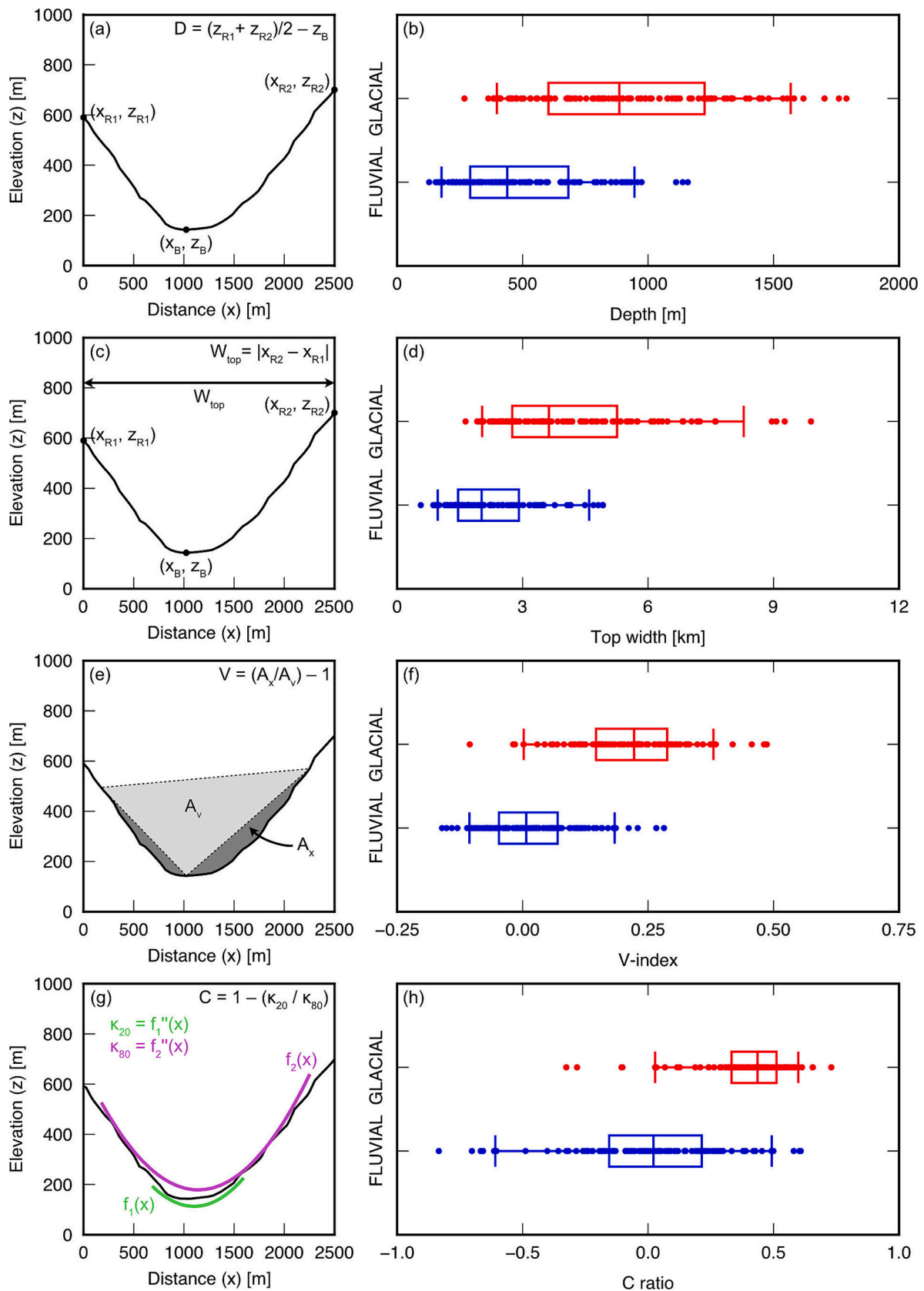


**Fig. 4.** Valley morphometric indices. Left panels illustrate the four metrics used to quantify valley cross-profile morphology. Right panels show the distribution of each metric across the fluvial and glacial valleys in the training dataset; boxplot marks the median, interquartile range, and 5th and 95th percentiles. (a, b) Valley depth ( $D$ ). (c, d) Valley top width ( $W_{top}$ ). (e, f) V-index ( $V$ ). Dark shaded region in panel e is the cross-sectional area of the valley at 80 % of the total relief; pale shaded region is the cross-sectional area of an idealised V-shaped valley. (g, h) Curvature ratio ( $C$ ). Coloured lines in panel g are second-order polynomials fitted to the valley cross-section at 20 % (green) and 80 % (purple) of the total relief.

where a, b, and c are constants. The curvature is then computed as

$$\kappa = \frac{d^2f}{dx^2} = 2a. \tag{6}$$

The curvature for each valley sub-section was normalised by multiplying by the width of the sub-section, such that curvature is scale-

independent and governed solely by valley shape (Prasicek et al., 2014). This allows for direct comparison between curvatures measured at different spatial scales.

In the training dataset, glacial valleys on average exhibit greater depths, widths, V-indices, and C ratios than fluvial valleys (Fig. 4). For glacial valleys, the median depth = 885 m, width = 3.63 km, V-index =

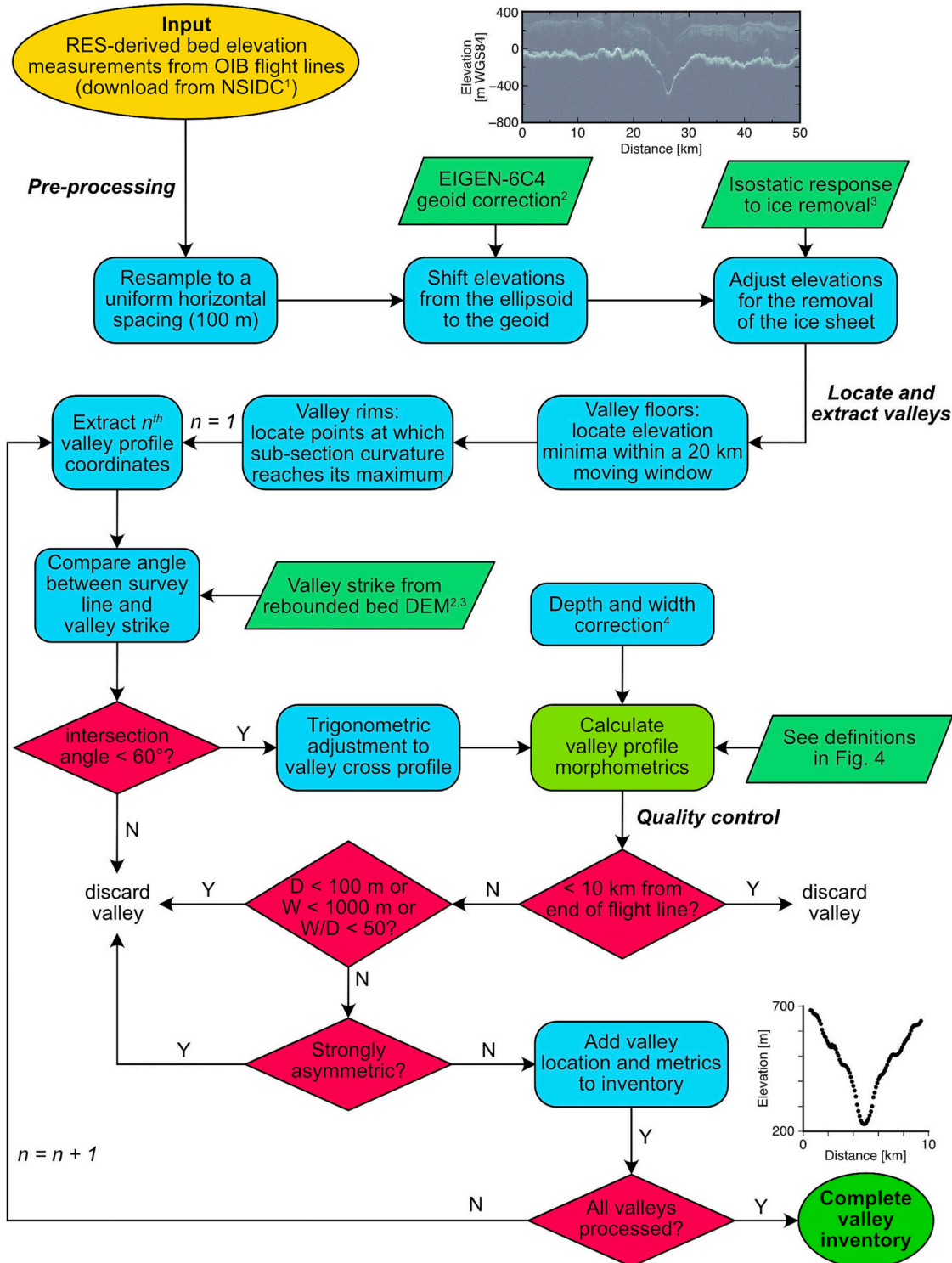


Fig. 5. Flow diagram for extracting subglacial valley cross-profiles from radio-echo sounding data. Symbology: ovals = start and end points; arrows = direction of movement; parallelograms = inputs; rectangles = processes; diamonds = decisions. Input datasets: 1 = NSIDC OIB bed picks (Paden et al., 2019); 2 = BedMachine bed elevation and geoid correction (Morlighem et al., 2017); 3 = isostatic response to modern GrIS removal (Paxman et al., 2022); 4 = correction for systematic underestimation of valley depth and width (Bartlett et al., 2020). An example radar echogram and extracted valley cross-profile are shown for illustration.

0.222, and C ratio = 0.436, whereas for fluvial valleys the median depth = 438 m, width = 2.02 km, V-index = 0.007, and C ratio = 0.021. Although the median values are distinct, there is overlap between the glacial and fluvial valley populations for all four metrics (Fig. 4). However, when valleys are plotted in multi-dimensional feature space, greater morphometric separability emerges (Fig. A1), highlighting the value of using multiple morphometric variables to classify valleys. Glacial valleys encompass a broader interquartile range of depths and widths than fluvial valleys, whereas the interquartile ranges for the V-index are comparable and for the C ratio fluvial valleys exhibit greater variance (Fig. 4).

For each cross-profile, we also computed two additional metrics: the exponent of a power law curve fitted to the valley cross-profile (Harbor and Wheeler, 1992; Pattyn and Van Huele, 1998) and the ratio between the top width and the valley width at 20 % of the total relief (Bull and McFadden, 1977). However, these metrics correlated very strongly with the V-index and/or C ratio and did not generate greater morphometric separability between glacial and fluvial valleys. We therefore limited our analysis to the four morphometrics illustrated in Fig. 4.

### 3.3. Automated extraction of Greenland valleys and their morphometrics from RES data

We identified subglacial valleys across Greenland using profiles of bed elevation derived from RES line data rather than from a continent-wide DEM such as BedMachine (Morlighem et al., 2017). This was because much of the smaller-scale geomorphological detail from the original RES data is lost or obscured during the DEM gridding process. In addition, significant artefacts can be introduced in the interpolation scheme that could be erroneously interpreted as real geomorphological features, especially in regions where survey line coverage is sparse or irregular. The strong spatial heterogeneity of the survey data used to construct BedMachine also causes the effective spatial resolution to vary significantly (Morlighem et al., 2017), which is unsuitable for geostatistical (machine learning) techniques. A limitation of using profiles of bed elevation from RES data alone is that features can only be detected where they intersect the flight tracks, which are often widely spaced and therefore do not provide a fully three-dimensional view of the topography. However, this issue was circumvented to a certain extent by focussing exclusively on subglacial valleys, which can be identified by, and classified according to, their cross-sectional profiles.

To automatically extract valleys and their morphometrics, we first applied a series of corrections (Fig. 5) to the pre-processed OIB MCoRDS Level 2 (2010–2019) and legacy CRISIS (2000–2009) bed pick data (Paden et al., 2019). CRISIS RES data were also acquired between 1993 and 1999, but the quality of these data is mixed, with significantly lower spatial resolution and greater bed elevation uncertainty than more recent datasets owing to less advanced radar systems (Gogineni et al., 2001). Given these issues and the limited spatial coverage of these survey years, we opted to omit them from our analysis. Although OIB RES profile data have a relatively consistent along-track resolution of ~20–30 m, all lines were resampled to a horizontal spacing of 100 m to ensure uniform resolution across the dataset and to closely align with the resolution of the training dataset valley profiles obtained from the Copernicus DEM. Bed elevations were then shifted from the WGS84 ellipsoid to the EIGEN-6C4 geoid (i.e., mean sea level) using the BedMachine geoid correction grid (Morlighem et al., 2017), and isostatically adjusted for the complete removal of the modern GrIS (Paxman et al., 2022) to correct for the exaggeration of relief caused by differential ice loading across valleys.

To extract valleys from the resampled and elevation-corrected line data, valley floors were identified as local topographic minima within a 20 km-wide moving window. When a 10 km window was used, more than double the number of ‘valleys’ were extracted, but most of these extra features were shallow (<100 m deep), reflecting smaller-scale bed roughness rather than distinct valleys. By contrast, use of a 40 km

window recovered relatively few valleys, with visual inspection of RES survey lines revealing that numerous valleys had been omitted due to proximity (<40 km) to deeper valleys. A value of 20 km was chosen as a trade-off between these competing factors. Following the identification of the valley floors, we located the valley rims by examining the curvature of the topography on either side of the valley floor. Specifically, we fitted a second order polynomial (Eq. (5)) to a sub-section profile centred on the valley floor. The width of the sub-section was incrementally increased, and we computed the curvature of the polynomial fitted to each successive sub-section (Eq. (6)). For a typical valley, the curvature will increase as the width of the sub-section increases, up to the point where the scale of investigation increases beyond the rims of the valley, whereupon the curvature will begin to decrease (Hilley et al., 2020; Prasicek et al., 2014). We therefore defined the valley rims as the points at the edges of the sub-section with the maximum curvature.

Since airborne geophysical surveys are not necessarily flown optimally relative to the orientation of subglacial topographic features, valley cross-sectional profiles viewed in RES data may be oblique to the ideal orthogonal profile. To correct for this effect, we estimated valley orientations using the rebounded BedMachine Greenland v.5 DEM (Morlighem et al., 2017; Paxman et al., 2022). For each valley, we determined the angular difference between the azimuth of the flight line and the valley strike (perpendicular to the valley orientation) and used a trigonometric correction to adjust the horizontal co-ordinates of the valley as if the survey line had been flown orthogonal to the valley orientation. If the azimuth of the flight line was highly oblique (>60°) to the valley strike, the valley was discarded since the true valley width would be overestimated by a factor of >2 and there is greater potential for distortion of the profile shape.

We then computed the four morphometrics (Fig. 4) for each valley using the adjusted distance-elevation co-ordinates. RES-derived bed elevation measurements have a typical vertical uncertainty of ~20 m (Paden et al., 2019), although RES data have a systematic bias towards underestimating valley depth and width by an average of ~30 m and ~560 m respectively due to off-nadir bed returns from the valley sides (Bartlett et al., 2020). We therefore applied a simple correction to each measured valley depth and width by adding these average offsets. Errors can also arise due to inaccurate picking of the bed reflection, although these are more difficult to quantify, not systematic, and unlikely to have a major impact on first-order valley morphology.

Finally, we carried out a series of quality control steps (Fig. 5). Valleys located <10 km from the ends of a flight line were discarded to remove potential artefacts. Strongly asymmetric features (where the height of the lower rim above the valley floor is less than one third of that of the higher rim) were also discarded. We permitted a minimum valley depth of 100 m, a minimum top width of 1000 m (after trigonometric adjustment), and a maximum width-to-depth ratio of 50. The minimum width value was selected to ensure that valleys were resolved by at least 10 co-ordinates. The depth and width-to-depth ratio thresholds were used to avoid sampling small-scale bed undulations or broad shallow depressions. The depth and width lower thresholds also match the lowest values recorded in the training data (Fig. 4), ensuring that the dataset of Greenland valleys does not contain features with dimensions beyond the training dataset range, thus avoiding extrapolation and spurious classifications.

### 3.4. Classification of Greenland valleys using supervised machine learning

To assign the valleys in Greenland to one of the two categorical classes used to label the training data (i.e., ‘glacial’ or ‘fluvial’), we used random forest classification (Breiman, 2001). As a supervised machine learning algorithm, the random forest predictive model was first trained using the morphometrics of the labelled valleys in the training dataset (Sections 3.1 and 3.2) and subsequently used to classify unlabelled valleys in Greenland (Section 3.3) based on the statistical similarity of their morphometrics to those of the training data.

A random forest comprises multiple individual decision trees, each built of a series of binary questions formulated from the independent variables (i.e., morphometrics) in the training data. For any valley with its combination of four morphometrics, the answers to the series of questions that form the tree will dictate its classification. A single tree is easy to construct, visualise, and interpret, but comprises only one permutation of the myriad possible sequences of binary questions and by necessity is often highly complex to accommodate the full variance of the training dataset. This ‘overfitting’ means the tree usually does not generalise well to the unlabelled dataset, leading to classification errors. A random forest circumvents this issue by using an ensemble of unique decision trees to add flexibility that results in improved classification accuracy. To ensure variation across the trees, bootstrap aggregation was used to draw (with replacement) a randomised set of valleys from the training dataset for each tree. Furthermore, every tree is grown using a random subset of morphometrics for each split, which results in more variation and less correlation between trees. The benefit of this approach is, by using many unique trees, potential outliers are smoothed out and the final decision structure is less variable and more reliable than a single decision tree.

Selecting the number of trees to use in the random forest is a trade-off between increased robustness and increased computation time, coupled with the diminishing rate of increased effectiveness as more trees are added. To determine the appropriate number of trees we computed the ‘out-of-bag’ classification error — the proportion of training samples that are misclassified having not been selected during the bootstrap aggregation process — as a function of the number of grown trees. We conservatively used 1000 trees in our ensemble and found that the error became relatively insensitive to the number of decision trees beyond 200 (Fig. A2). To further test the performance of the random forest classifier, we performed ten-fold cross validation on the training data. This technique involves randomly assigning all the training data into 10 equally sized bins; the random forest model is trained on nine of the bins, and then the trained model is used to classify the valley profiles in the remaining 10th (testing) bin. This process is repeated 10 times (‘folds’), such that each bin has been utilised as the testing bin. The classes assigned to the test data are compared to their true labels, and the results are aggregated to produce an overall prediction error.

After model training and cross validation, we passed each unlabelled Greenland valley through the ensemble of 1000 trees in the random forest. Each tree ‘votes’ for a classification of ‘fluvial’ or ‘glacial’ and the result is aggregated from each of the individual predictions, with each valley assigned a predicted class based on the majority ‘vote’ across all 1000 trees. For any given valley, the number of trees predicting each of the two classes gives a measure of classification probability or likelihood, while the out-of-bag classification error and cross validation error are indicators of the overall model classification accuracy.

## 4. Results

When describing spatial patterns in valley locations, morphometrics, and classification across Greenland, we refer primarily to the eight major GrIS drainage basins (Zwally et al., 2012) labelled in Fig. 1a and subsequent figures. These catchments are abbreviated as follows: NO = north; NE = northeast; CE = central east; SE = southeast; SO = south; SW = southwest; CW = central west; NW = northwest.

### 4.1. Spatial distribution and morphometrics of subglacial valleys

Across Greenland, we extracted the morphometrics of 5335 valley cross-profiles that met our quality control criteria (Fig. 5). The spatial distribution of mapped valleys across the island is strongly heterogeneous; valleys are most frequently observed in near-coastal regions, and are comparatively rare in the interior, particularly in inland areas of the NO, NE, and NW catchments (Fig. 6). This distribution primarily reflects the heterogeneity in RES data coverage, which shows a bias towards

oversampling near-coastal areas and undersampling interior areas relative to the distribution of land across Greenland as a whole (Fig. 6f, g). However, RES data coverage is sufficient (Fig. 1b) to exclude the possibility of extensive valley systems being undetected in the interior.

Around the margins, valleys are widespread in the chain of mountainous terrain that runs along the eastern margin of the CE, SE, and SO catchments, as well as along the lower lying margins of the NO, NE, SW, CW, and NW catchments (Fig. 6), which are drained by major outlet glacier systems including Humboldt, Petermann, NEGIS, and Ilulissat (Jakobshavn) (Fig. 1a; A3). While some of these valley networks have been mapped using regional-scale geophysical analysis and are readily visible in the BedMachine DEM, e.g., in the NO and CW catchments (Cooper et al., 2016; Livingstone et al., 2017; Morlighem et al., 2017), others have not previously been documented and are less conspicuous in BedMachine. These omissions may in part be due to large and irregular gaps between RES survey lines (Fig. 1b) and because valley scale and orientation may be inconsistent with the modern ice velocity, meaning both mass conservation and streamline diffusion techniques will omit or not fully resolve many of these features. Valleys are widespread across southern Greenland but comparatively sparse in the interior of northern Greenland (Fig. 6); the valleys in this region are likely linked to the Petermann ‘mega-canyon’ and its inland tributary network (Bamber et al., 2013; Paxman et al., 2021). The first-order spatial distribution of valleys is reflected in the subglacial topographic roughness, which is elevated in regions of high valley density (e.g., the eastern highlands and the western margin), and lowest in the interior of central and northern Greenland (Cooper et al., 2019).

The deepest valleys, with relief of up to 2.5 km, are located primarily within the highlands of the CE catchment (Fig. 6a). Valleys with depths exceeding 1 km are also found in the highlands of the SE, SO, and NO catchments, as well as parts of the SW, CW, and NW catchments that are close to the ice margin (Fig. 6a). Valleys across the interior are typically characterised by lower relief, with depths often <400 m (Fig. 6a). The widest valleys, with widths of >8 km, are typically found in the highlands of the CE and SE catchments (Fig. 6b). Large valley widths are also observed in the lower-lying CW catchment; many of these valleys are comparatively shallow (Fig. 6a), implying a greater width-to-depth ratio than valleys in CE and SE regions. The NE and NW catchments are characterised by the narrowest valleys, commonly <4 km across (Fig. 6b). Regions containing valleys with a high V-index (>0.4) include the highlands of the CE, SE, and NO catchments, as well as parts of the CW margin (Fig. 6c). Valleys with a lower V-index are observed in the NW catchment and in lower-lying interior areas of all northern catchments (Fig. 6c). Valleys with a high curvature ratio (>0.6) are found in many near-coastal areas, with a general trend towards smaller curvature ratios predominating further into the continental interior (Fig. 6d).

### 4.2. Subglacial valley classification

Of the 5335 mapped valleys, the random forest model classified 3676 as ‘glacial’ and 1659 as ‘fluvial’ (Fig. 7a). Each valley was scored between 0 and 1, where 0 reflects a valley that is classified as ‘fluvial’ by all decision trees in the random forest, 1 reflects a valley that is classified as ‘glacial’ by all trees, and (e.g.) 0.5 reflects a valley classified as ‘glacial’ by half the trees and ‘fluvial’ by the other half. The score is therefore a measure of the likelihood of a valley being ‘glacial’ in origin. To aid interpretation, we differentiate between ‘high probability’ and ‘low probability’ valleys, with ‘high probability’ valleys having a score of <0.25 (‘fluvial’) or >0.75 (‘glacial’) and ‘low probability’ valleys having scores of between 0.25 and 0.50 (‘fluvial’) or 0.50 and 0.75 (‘glacial’) (Fig. 7). These thresholds are somewhat arbitrary but help differentiate between valleys which lie distinctly inside the morphometric space of fluvial/glacial valleys within the training dataset and those which plot in regions of morphometric overlap or in morphometric space that is not strongly represented in the training dataset (see Section 5).

Across Greenland, clusters of high probability ‘glacial’ valleys are

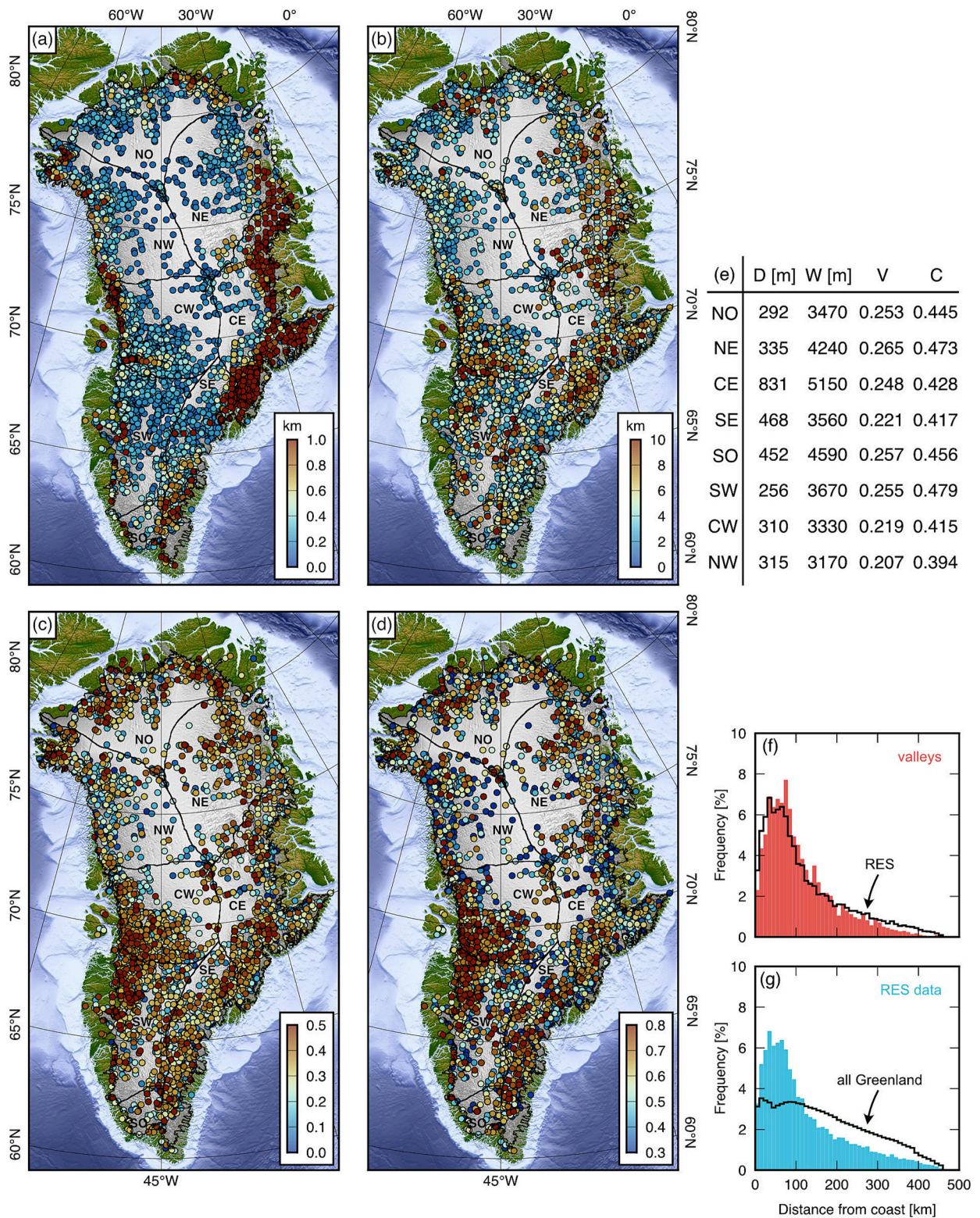


**Fig. 6.** Valley morphometrics across Greenland. Circles marking the subglacial valleys are coloured according to the four selected morphometrics. (a) Valley depth, (b) valley width, (c) V-index, (d) curvature ratio. In areas of dense valley coverage, overlapping circles are overlain in ascending numerical order for each metric. (e) Table of mean valley morphometrics for each ice sheet catchment. (f) Frequency distribution of the distance of valleys from the coast. Black line shows the outline of the frequency distribution for all RES survey datapoints. (g) Frequency distribution of the distance of all RES-derived bed elevation measurements from the coast. Black line shows the outline of the frequency distribution for all land in Greenland.

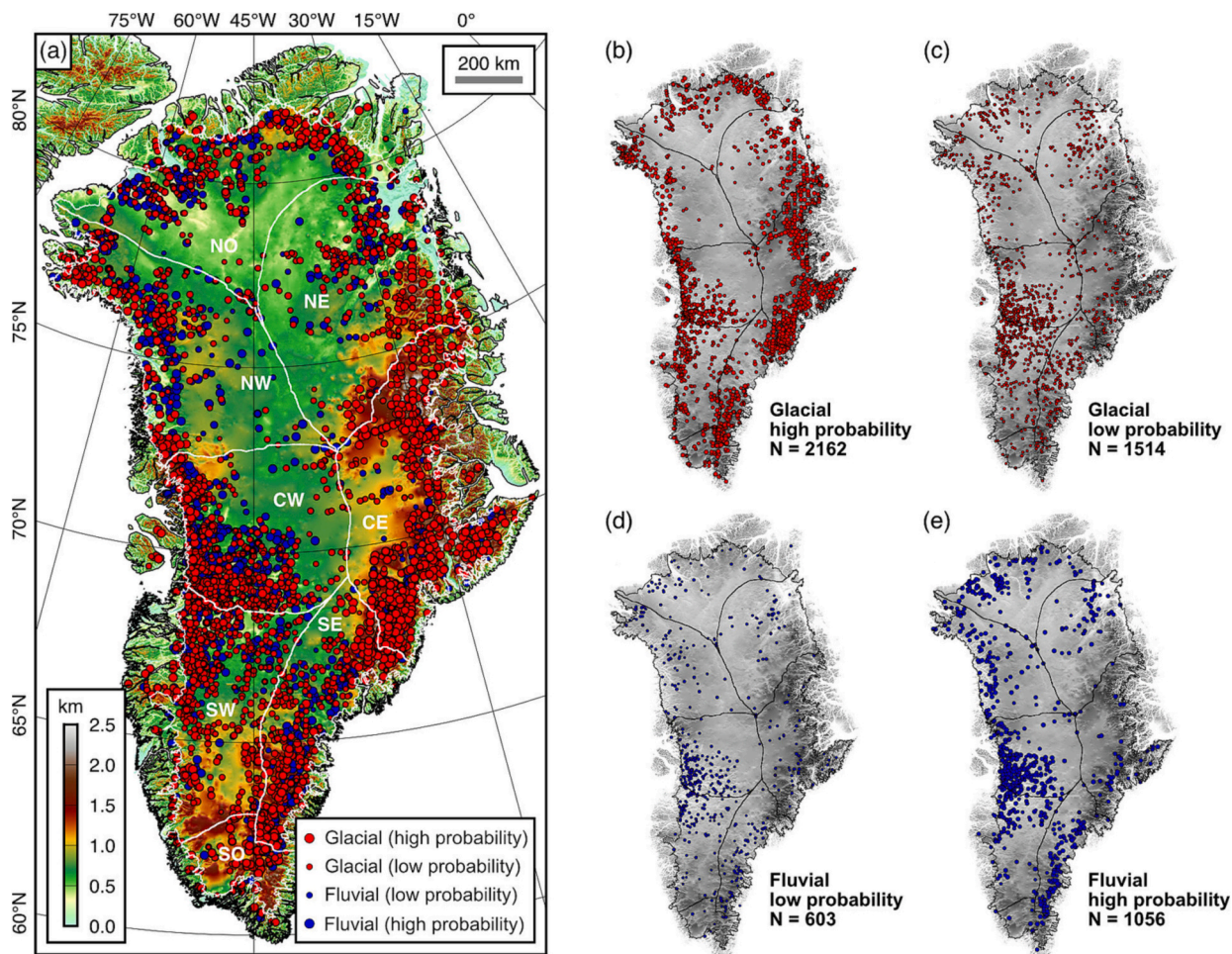


**Fig. 7.** Valley classification using random forest. (a) Spatial distribution of valleys classified as ‘glacial’ (red circles) or ‘fluvial’ (blue circles) using the random forest model. Circle radii are scaled to the probability of each valley belonging to its assigned class. Bed elevations are relative to mean sea level and are isostatically adjusted for the removal of the modern ice load (Morlighem et al., 2017; Paxman et al., 2022). (b) High probability ‘glacial’ valleys (score > 0.75). (c) Low probability ‘glacial’ valleys (0.50 < score < 0.75). (d) Low probability ‘fluvial’ valleys (0.25 < score < 0.50). (e) High probability ‘fluvial’ valleys (score < 0.25).

observed in the high elevation terrain found in the NO, CE, SE, and SO catchments, as well as marginal areas in the lower-lying CW and SW catchments (Fig. 7b). These high probability ‘glacial’ valleys can be seen to correspond to regions characterised by elevated D, W, V, and C values (Fig. 6). By contrast, low probability ‘glacial’ valleys are more broadly distributed across Greenland, with moderate clustering in the SW and CW catchments (Fig. 7c). High probability ‘fluvial’ valleys are most commonly located in the CW, NW, and NO catchments, with a number of high and low probability ‘fluvial’ valleys distributed across the low-lying continental interior (Fig. 7d,e). Clusters of ‘fluvial’ valleys are also located along the spine of the high topography that runs north-to-south in the SE catchment (Fig. 7e).

Geographically, the regions with the highest (i.e., most ‘glacial’) average valley scores are the highlands located in the NO, CE, SE, and SO catchments, as well as areas proximal to the ice margin along western Greenland (Fig. 8a,b). While ‘glacial’ valleys are universally more common than ‘fluvial’ valleys (Fig. 8c), the frequency of ‘fluvial’ valleys relative to ‘glacial’ valleys is highest in the NO, NE, CW, and NW catchments (Fig. 8c). Indeed, the lowest (i.e., most ‘fluvial’) average valley scores are observed in the interior of the northern half of Greenland, as well as in parts of the SE catchment (Fig. 8a,b). These catchments exhibit mean valley scores close to 0.5 (Fig. 8d), but with a broad interquartile range that reflects the high degree of short-wavelength variability in the regional average (Fig. 8b).

Regarding random forest model performance, we found a ten-fold

cross validation error rate of 0.06 for the training data, corresponding to a classification accuracy of 94%. We also found that the classification of out-of-bag training samples in the full dataset (i.e., those not selected during bootstrap aggregation) levelled out at  $\sim 0.06$  for >200 trees (Fig. A2). Out-of-bag errors also provide an opportunity to assess the relative importance of each of the four morphometric variables (Grömping, 2009) (i.e., how much ‘influence’ each variable has upon valley classification). We found that valley width ( $W_{top}$ ) had the greatest feature importance, with the other three variables (D, V, and C) having high and approximately equal importance (80–84% of that of  $W_{top}$ ; Fig. A2), underlining the value of incorporating all four metrics. The intercorrelation between the four valley morphometrics across the full dataset is generally low, with the strongest inter-variable correlation coefficients observed between D and  $W_{top}$  (0.53) and V and C (0.66) (Fig. A2). Given that depth and width measure valley scale, while the V-index and curvature ratio measure valley shape, these positive inter-correlations are to be expected (Fig. A1) but are sufficiently low that each of the four metrics retains a high importance and therefore adds value to the classification (Fig. A2).

Due to the nature of the OIB mission, certain valleys are sampled by repeat survey tracks flown during multiple field seasons (MacGregor et al., 2021). This provides a further opportunity to assess the reliability of our valley extraction algorithm and random forest classification model by comparing the class and score of valleys that are sampled multiple times. Across all repeat-sampled valleys (defined as a valley

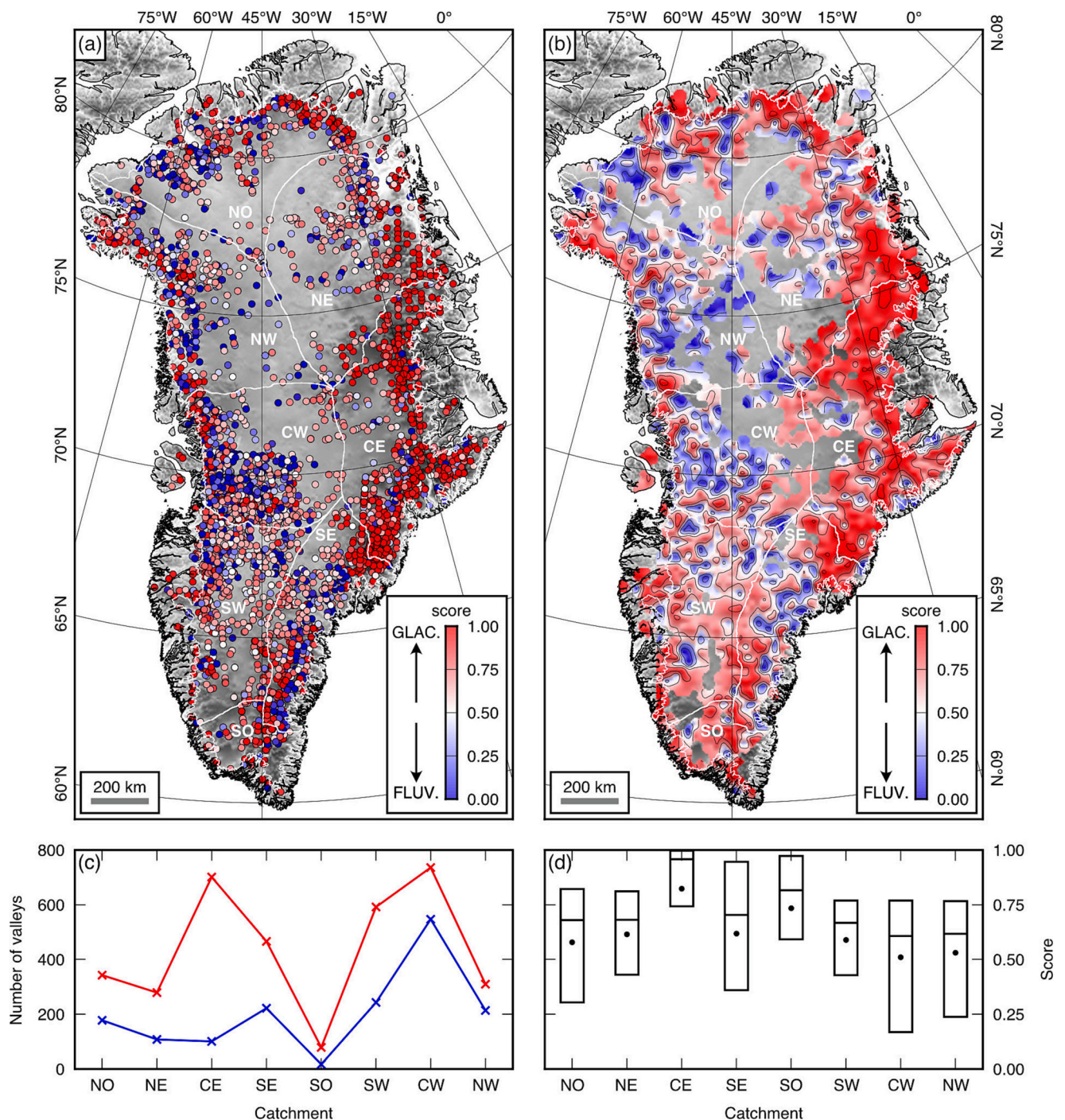


**Fig. 8.** Valley classification scores. (a) Valleys coloured according to their 'score' assigned by random forest classification. The score is defined as the proportion of decision trees in the random forest that classified each valley as 'glacial' (i.e., a score of 1 indicates unanimously 'glacial' and 0 indicates unanimously 'fluvial'). (b) Gridded scores. Valley scores were averaged over a 25 km moving window and subsequently interpolated onto a grid mesh using a tensional spline and smoothed using a 25 km Gaussian filter. Contour interval is 0.2. Areas >25 km from the nearest valley were masked to remove spurious extrapolation. (c) Number of 'glacial' (red) and 'fluvial' (blue) valleys recorded in each ice catchment. (d) Boxplots of valley classification scores in each catchment. Note that 5th and 95th percentile tails are not displayed since they span the entire range of possible scores in each catchment.

located within 100 m of any other), we found a classification mismatch rate of 0.16 (i.e., the same valley, when sampled multiple times, received the same classification 84 % of the time). However, the median 'swing' in valley score was 0.06, implying that repeat-surveyed valleys that received different classifications typically had small majorities, with a small shift in the proportion of trees 'voting' for each class sufficient to change the overall result. We therefore advise that caution should be taken to avoid overinterpretation of the classification of

valleys whose score is close to 0.5.

## 5. Discussion

In this section, we aim to examine the first-order relationships between valley distribution and morphology and contemporary glacial dynamics, and the implications for the mode(s) and relative timing of formation of valley networks across Greenland.

### 5.1. Patterns of glacial valley incision

Continental ice sheets are capable of intensive selective erosion beneath fast-flowing, warm-based ice and contemporaneous preservation beneath slow-flowing, cold-based ice (Jamieson et al., 2008; Sugden and John, 1976). To examine whether the ‘glacial’ valleys identified using random forest classification are consistent with erosion beneath the modern-day GrIS, or whether they are likely being preserved beneath the modern ice sheet and therefore indicative of glacial valley incision earlier in its history, we computed a simplistic ‘preservation potential’ metric of the modern GrIS at the location of each high probability ‘glacial’ valley. For simplicity, we excluded the low probability ‘glacial’ valleys, whose origin is more uncertain (see Section 4.2), from this analysis.

We defined ‘preservation potential’ using the measured ice surface velocity (Joughin et al., 2018) and inferred likely basal thermal state of the ice sheet (MacGregor et al., 2022) (Fig. A3), which synthesises basal properties such as temperature, slip ratio, melt rate, and presence of liquid water, as inferred from borehole observations, radio-echo sounding, and ice sheet models. Although glacial erosion rates are

likely dependent on a number of other variables including climate, bedrock lithology, and orientation of bed topography relative to ice flow, relationships between these factors and glacial erosion rates remain poorly quantified (Alley et al., 2019; Cook et al., 2020). Given these limitations, any definition of the ‘preservation potential’ will be somewhat arbitrary, so we delineate three simple levels:

1. Low – either (a) basal thermal regime is likely thawed and surface velocity is  $>50$  m/yr or (b) basal thermal regime is uncertain and surface velocity is  $>200$  m/yr.
2. Medium – either (a) basal thermal regime is likely thawed and surface velocity is  $<50$  m/yr or (b) basal thermal regime is uncertain and surface velocity is between 50 and 200 m/yr.
3. High – either (a) basal thermal regime is likely frozen or (b) basal thermal regime is uncertain and surface velocity is  $<50$  m/yr.

When these criteria are applied, ‘glacial’ valleys with a low preservation potential, indicating likely modification beneath the modern GrIS, are primarily located beneath the warm-based, fast-flowing ice streams and outlet glaciers located in the SW, CW, and NE catchments,

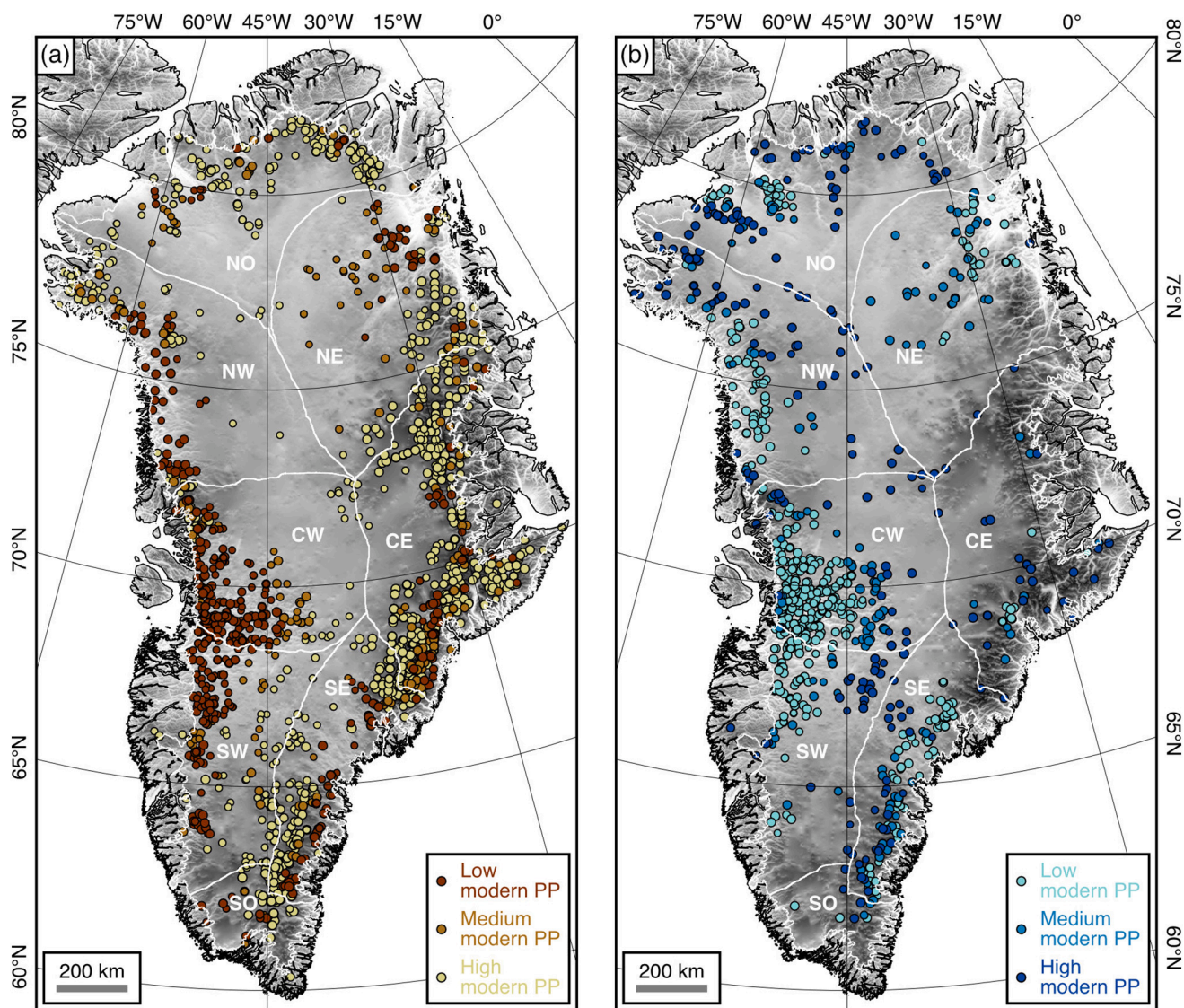


**Fig. 9.** Preservation potential of valleys beneath the Greenland Ice Sheet. (a) High probability ‘glacial’ valleys. (b) High probability ‘fluvial’ valleys. Preservation potential (PP) is determined according to the measured ice surface velocity and likely basal thermal state (Joughin et al., 2018; MacGregor et al., 2022). Low preservation potential valleys have likely been modified by the modern GrIS; high preservation potential valleys are likely preserved beneath the modern GrIS and reflect incision prior to, or during earlier stage(s) of, glaciation. Circle radii are scaled to the probability of each valley belonging to its assigned class.

as well as ice-marginal areas of the CE, SE, and NW catchments (Fig. 9a). This is consistent with high erosion rates that have been inferred for glacial catchments along the western margin of Greenland, particularly in low-lying regions (Cowton et al., 2012; Strunk et al., 2017). 'Glacial' valleys with a high preservation potential are concentrated in the NO, CE, SE, and SO catchments, most conspicuously within the chain of rough, mountainous terrain along the eastern margin (Fig. 9a). Since these valleys are primarily located in high mountainous terrain and currently covered by cold-based ice, we suggest that their origin may be related to valley incision during period(s) of Greenland's glacial history when ice extent was more restricted and confined to high elevation areas (Dolan et al., 2015; Koenig et al., 2015; Schaefer et al., 2016; Solgaard et al., 2011).

## 5.2. Fluvial valley preservation and modification

Classification of a valley as 'fluvial' is potentially indicative of a lack of significant modification beneath the modern GrIS or past ice sheets. There are three possible scenarios that might explain the presence of 'fluvial' valleys.

The first scenario is that some of these valleys were incised by river systems under ice-free conditions, for example prior to large-scale ice growth and/or during interglacial periods where ice extent was significantly reduced. These valleys would have subsequently been preserved beneath cold-based, non-erosive ice associated with negligible long-term (million-year timescale) erosion rates, as has been documented in Antarctica (Baroni et al., 2005; Franke et al., 2021; Rose et al., 2013) and using radionuclide analysis from preserved basal soil at the GISP2 core site in central Greenland (Fig. 1b) (Bierman et al., 2014). This situation most likely applies to the high preservation potential 'fluvial' valleys located in the NW and NO catchments, in the inland reaches of the central and southern catchments, and along parts of the highlands of eastern Greenland (Fig. 9b). The presence of these valleys may therefore be diagnostic of localised long-term preservation of pre- and/or interglacial landscapes, suggesting that average glacial conditions (Porter, 1989) in these areas have been ice-free and/or cold-based (i.e., lacking in fast-flowing, warm-based ice) over the history of the GrIS. The lack of a clear glacial overprint in the interior of northern Greenland suggests that during past transitions between glacial states (e.g., local- vs. continental-scale), the GrIS advanced/retreated without subjecting this region to significant erosion, which may be indicative of a cold-based ice margin or a fast-advancing/retreating warm-based margin.

The second scenario concerns the clusters of 'fluvial' valleys that are located beneath ice that is currently fast-flowing and/or warm-based and thus have a low preservation potential, as found along the margins of the NE, SW, CW, and NW catchments (Fig. 9b). Palaeo-fluvial drainage networks have previously been identified in these regions, including the Ilulissat system in central west Greenland (Cooper et al., 2016; Jess et al., 2020). The presence of these 'fluvial' valley networks is somewhat counterintuitive, given that the overlying glaciological conditions do not appear to be conducive to landscape preservation. However, we note that these catchments also contain many 'glacial' valleys and a wide range of valley classification scores (Fig. 8c,d), which may suggest that the long-term average glacial conditions experienced by these valleys have facilitated selective overprinting of an inherited pre-glacial valley network while allowing elements of the original fluvial signature, including dendritic planforms, V-shaped cross-sections, and concave-up longitudinal profiles, to be retained (Cooper et al., 2016; Livingstone et al., 2017).

Possible reasons for this partial preservation of fluvial valley networks beneath contemporary fast-flowing, warm-based ice streams may include (i) the relatively distributed and topographically unconfined nature of the ice flow, for example along the western margin (Fig. A3), which may render it less capable of localised valley cross-profile modification, (ii) valley alignment that is not optimal for incision; many valleys in the Ilulissat catchment are oriented obliquely to ice flow

(Cooper et al., 2016; Jess et al., 2020), which may inhibit valley modification, and/or (iii) some ice streams may be relatively short-lived and/or highly temporally variable, as has been suggested for NEGIS (Franke et al., 2022a), such they have had a lesser integrated erosive impact on the landscape than would be expected if their modern dynamics were extrapolated back in time. The pattern of 'fluvial' valleys may therefore provide insights into the timescales of existence of certain contemporary ice streams, although quantification of these timescales is beyond the scope of this study.

The third scenario is that some 'fluvial' valleys may have been misclassified due to biases present in the training dataset, for example if it is not fully representative of valley morphology in Greenland. If we compare the morphometrics of valleys in the training data to those in Greenland, the median Greenland V and C values are close to those of the glacial valleys in the training dataset (Table A1), which likely accounts for the dominance of valleys classified as 'glacial' (N = 3676) compared to 'fluvial' (N = 1659), but the training dataset appears to be broadly representative of the Greenlandic valleys (Fig. A4). However, valleys in Greenland do exhibit a wider range of V and/or C values, which may lead to some misclassification as supervised machine learning models such as random forest do not extrapolate well beyond the range of the training data (Elmes et al., 2020). Misclassification may also arise because the training dataset does not include valleys such as steep-sided canyons or U-shaped valleys that can be carved by rivers, particularly in certain lithologies (Rogers and Engelder, 2004). This issue may apply to the Petermann 'mega-canyon' in northern Greenland, which is believed to be of fluvial origin (Bamber et al., 2013) but is classified as 'glacial' by our random forest model; this likely reflects a lack of representation of canyon-like fluvial valleys in the training dataset. Development of more targeted training datasets in the future will help resolve these region-specific ambiguities.

## 5.3. Role of other valley-forming processes

The preceding section raises an important limitation regarding valley classification in Greenland: many valleys will likely have experienced erosion by a combination of ice and water and therefore binary classification of valleys as either 'glacial' or 'fluvial' is oversimplistic. We also highlight that other processes not explicitly considered in the training dataset may be responsible for valley incision. For example, subglacial meltwater may cause steady-state incision of tunnel valleys through seasonal flow and/or rapid incision during abrupt stochastic flood events (Beaud et al., 2018; Chambers et al., 2020; van der Vegt et al., 2012).

Subglacial meltwater channels were not considered explicitly in the training dataset owing to the relative lack of consensus regarding the physical processes responsible for their development and the less diagnostic nature of their cross-sectional profiles (Lelandais et al., 2016; van der Vegt et al., 2012). Instead, these channels tend to be most readily identified through their undulating longitudinal profiles and/or parallel planform drainage patterns that align with the ice surface gradient (Grau Galofre and Jelinek, 2017; Kirkham et al., 2022; Livingstone et al., 2017; Sugden and John, 1976), which often cannot be adequately resolved using RES data alone, particularly where coverage is sparse. We emphasise therefore that since our training dataset was established with the aim of identifying the morphometric signatures of valley incision by rivers and glacial ice, a 'fluvial' or 'glacial' classification does not preclude a role for subglacial meltwater erosion.

Although disentangling the imprints of erosion by glacial ice vs. subglacial water vs. rivers is complex, we can examine the mapped valley morphometrics to identify areas where subglacial meltwater is relatively more or less likely to have exerted an influence on valley morphology. To do so, we used a series of criteria to identify features that resemble tunnel valleys formed by subglacial meltwater. These criteria are: (i) a maximum depth of 500 m and a maximum width of 5 km, based on reported upper limits (van der Vegt et al., 2012). (ii) A

width-to-depth ratio between 5 and 25, allowing for a typical value of  $\sim 10$  with higher values also reported (van der Vegt et al., 2012). (iii) A V-index and C ratio of at least one standard deviation below the respective mean values across Greenland (Table A1). This allows for the observation that tunnel valley cross profiles can take a range of forms, including V-shapes, U-shapes, inner gorges, and box-shapes, with U-shapes typically the most common (van der Vegt et al., 2012). (iv) A classification score of between 0.25 and 0.75, indicating that the valley does not fit definitively into either fluvial or glacial morphometric space, reflecting the observation that fluvio-glacial processes and subglacial meltwater channels can create hybrid valley forms (Livingstone et al., 2017).

In addition, we compared valley locations to the predicted pattern of hydrological flow routing beneath the GrIS. To calculate the subglacial hydrological network, we computed the hydrological potential that is assumed to drive subglacial water flow (Shreve, 1972)

$$\phi = \rho_w g Z_b + \rho_i g (Z_s - Z_b) \quad (7)$$

where  $\rho_w$  and  $\rho_i$  are the densities of water ( $1000 \text{ kg m}^{-3}$ ) and ice ( $917 \text{ kg m}^{-3}$ ), respectively, and  $g$  is the acceleration due to gravity ( $9.81 \text{ m s}^{-2}$ ). The bed ( $Z_b$ ) and surface ( $Z_s$ ) elevation were derived from BedMachine v.5 (Morlighem et al., 2017). All hydrological minima (sinks) in the hypopotential field were filled to allow continuous flow to the edges of the model domain. The flow direction was calculated from this filled hypopotential model, and the flow accumulation was computed as the total number of upstream cells feeding any given point. We assumed an arbitrary flow accumulation threshold of 1000 cells to define a hydrological pathway; at the 150 m horizontal resolution of the BedMachine DEM, this threshold corresponds to an upstream drainage area of  $22.5 \text{ km}^2$ . Finally, we did not permit any hydrological pathways in regions where the basal thermal state of the ice sheet is 'likely frozen' (MacGregor et al., 2022). We imposed the condition that valleys potentially acting as conduits for subglacial meltwater must be located within 10 km of the nearest hydrological pathway, which allows for uncertainty in the bed and surface elevation fields.

Valleys that meet the criteria of being morphometrically consistent

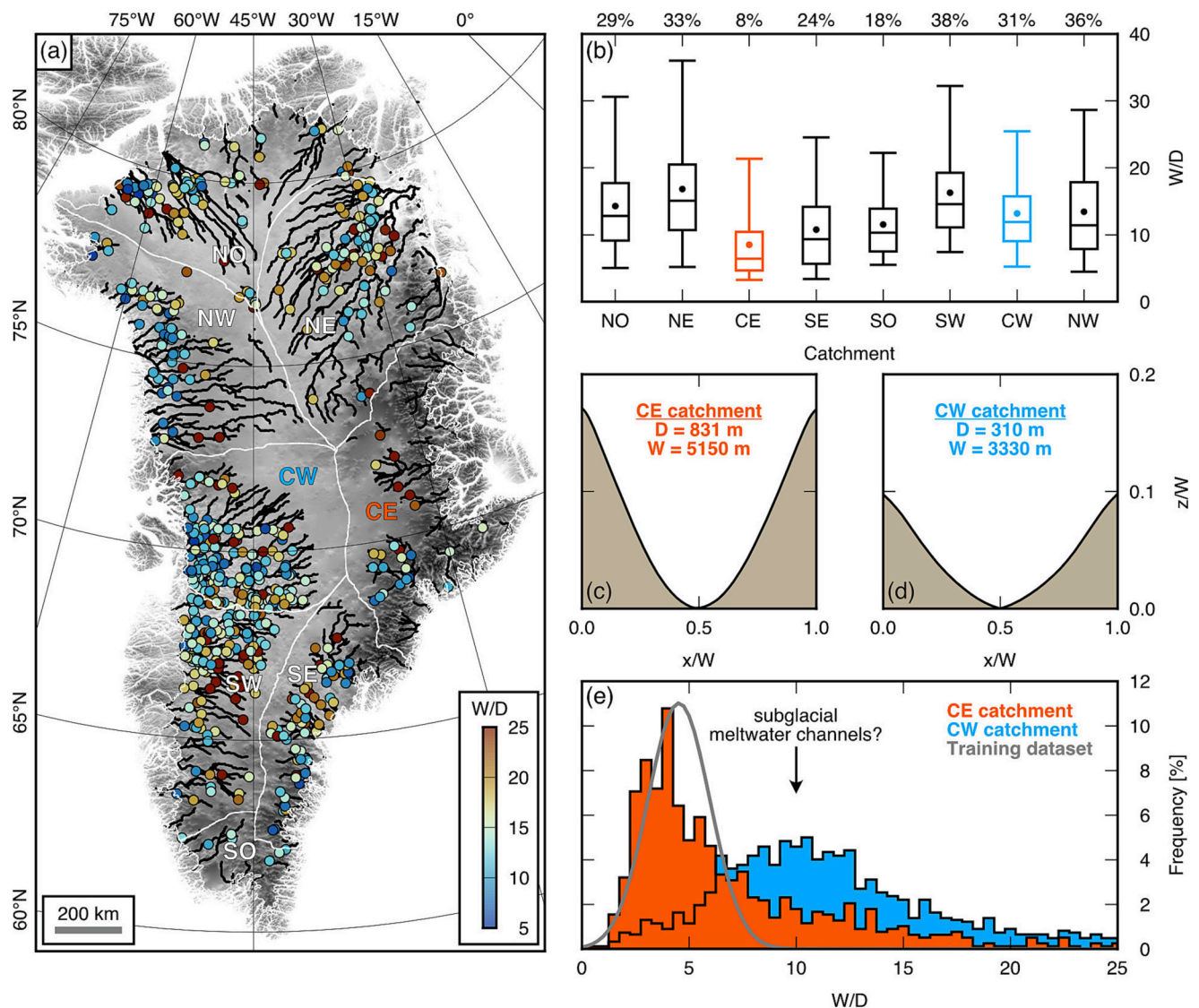


**Fig. 10.** Role of subglacial meltwater in valley development. (a) Valleys that meet the criteria of having been potentially incised by subglacial meltwater. Colour scale shows the width-to-depth ratio. Black lines mark hydrological pathways (flow accumulation  $> 1000$  upstream cells). (b) Boxplots of valley width-to-depth ratio. Percentages reflect the proportion of valleys in each catchment that meet the criteria of having been potentially incised by subglacial meltwater. (c) Average valley cross profile in the CE catchment. (d) Average valley cross-profile in the CW catchment. Horizontal and vertical co-ordinates have been normalised by the valley width. Average valley depth (D) and width (W) across the catchment are labelled. (e) Frequency distribution of valley width-to-depth ratio in the CW and CE catchments. Grey curve indicates the normal distribution associated with the training dataset.

with subglacial meltwater valley incision are primarily located in the NO, NE, SW, and CW catchments (Fig. 10a), specifically in the upstream areas of the Ilulissat, NEGIS, Humboldt, and Petermann outlet glaciers. This finding supports previous inferences of the presence of subglacial meltwater channels in these regions (Andrews et al., 2015; Chandler et al., 2018; Franke et al., 2020; Livingstone et al., 2017). By contrast there are very few valleys resembling tunnel valleys in CE, SE, and SO Greenland (Fig. 10a); these areas are characterised by the lowest average width-to-depth ratios (Fig. 10b). Comparing the frequency distribution of valley width-to-depth ratios in the CE catchment to the training dataset, both show a clear modal peak at around 4–5, with the CE catchment valleys showing a small ‘tail’ beyond the range of the training dataset (Fig. 10c,e). By contrast, valleys in the CW catchment exhibit a larger average width-to-depth ratio (Fig. 10b,d), with a modal peak at 8–12, which aligns well with values typical of tunnel valleys (van der Vegt et al., 2012), and a broad range extending well beyond that of the training data (Fig. 10e). This indicates that the training dataset is not fully representative of valleys in the CW catchment, as is also the case for parts of the NO, NE, and SW catchments (Fig. 10b).

We therefore suggest that future applications of machine learning approaches to subglacial landscape analysis could be expanded by integrating cross-profile morphometrics of glacial, fluvial, and subglacial tunnel valleys with valley planform characteristics (Grau Galofre and Jellinek, 2017). This could be applied to regions where dense spatial coverage of RES data allows valley planform geometry to be accurately quantified, for example in near-marginal areas of western or northern Greenland (Fig. 1b). Although data coverage is sufficient for this study, the valley inventory could also be expanded to other recent (non-OIB) RES surveys (e.g., Franke et al., 2022b). Moreover, we note that automated methods of valley mapping across Greenland have other potential applications beyond the scope of this study. For example, geostatistical comparisons could be made between landscapes exposed around the margins of Greenland and those covered by the ice sheet, relationships between valley morphology and subglacial geology could be explored, and these methods could be applied to subglacial landscapes in Antarctica or on other terrestrial bodies in the solar system. Machine learning methods extending beyond random forest and other classifiers, including deep learning algorithms based on artificial neural networks, could potentially be employed to help address these more complex applications.

## 6. Conclusions

In this study, we have used a combination of automated mapping from RES data and random forest classification to examine patterns in the distribution and morphology of subglacial valleys across Greenland. We draw the following conclusions:

1. We extracted 5335 subglacial valleys from the Operation IceBridge and legacy CReSIS RES survey data, of which 3676 were classified as ‘glacial’ and 1659 as ‘fluvial’ based on morphometric comparison with the training dataset of valleys from subaerial landscapes in the Northern Hemisphere.
2. Many ‘glacial’ valleys along the western margin of Greenland are consistent with active incision beneath modern day ice streams. By

contrast, the high elevation terrain in eastern and southern Greenland contains ‘glacial’ valleys preserved beneath slow-flowing, cold-based areas of the contemporary GrIS; these valleys were likely incised beneath a different ice configuration that existed earlier in Greenland’s glacial history. The implications of these valleys for the past behaviour of the GrIS will be explored in a future study.

3. Valleys bearing hallmarks of a fluvial origin are identified in the low-lying interior of northern and central Greenland and in areas of high subglacial terrain, indicating that negligible long-term erosion rates in these regions have facilitated the preservation of pre-glacial and/or inter-glacial landscapes beneath the ice over timescales on the order of  $10^5$ – $10^6$  years.
4. The lower-lying areas of western and northeastern Greenland contain valley networks that exhibit a broad continuum of morphologies, which likely reflects a complex erosive history, involving interactions between fluvial valley inheritance, selective erosion by ice, and incision by subglacial meltwater.

## Declaration of competing interest

The authors declare the following financial interests/personal relationships which may be considered as potential competing interests:

Guy Paxman reports financial support was provided by the Leverhulme Trust.

## Data availability

The Copernicus GLO-90 digital elevation model was accessed via OpenTopography (<https://doi.org/10.5069/G9028PQB>). The Operation IceBridge MCoRDS Level 2 ice thickness (<https://doi.org/10.5067/GDQ0CUCVTE2Q>) and BedMachine version 5 (<https://doi.org/10.5067/GMEVBWFLWA7X>) datasets were accessed via the National Snow and Ice Data Center. The isostatic response to the unloading of the modern Greenland Ice Sheet was accessed via the Arctic Data Center (<https://doi.org/10.18739/A2280509Z>). The valley cross-profile training dataset assembled for this study and the resulting classified dataset of Greenland valleys can be found at <https://doi.org/10.5281/zenodo.7794565>. The code used to extract valleys from the OIB RES data, calculate valley cross-profile morphometrics, and classify valleys using the trained random forest model can be found at <https://doi.org/10.5281/zenodo.7797717>.

## Acknowledgements

This research was funded by a Leverhulme Trust Early Career Fellowship, grant number ECF-2021-549. GJGP would like to thank Mike Bentley, Fiona Clubb, Ian Evans, Stewart Jamieson, Joe MacGregor, Steven Palmer, and Kirsty Tinto for helpful discussions at various points during the development of this manuscript. The author also extends thanks to the members of the Lamont-Doherty Earth Observatory Sea Level group, discussions with whom inspired the initial undertaking of this research. Figures were prepared using the Generic Mapping Tools (GMT) version 6 software package (Wessel et al., 2019).

## Appendix A

Table A1

Descriptive statistics for morphometric indices of valleys in the training dataset and from Greenland.

Metric	Setting	Count	Mean	Standard deviation	Median	5th percentile	95th percentile
Depth (m)	Glaciated	100	919	375	885	397	1570
	Fluvial	100	506	257	438	176	946
	Greenland	5335	413	379	264	112	1300

(continued on next page)

Table A1 (continued)

Metric	Setting	Count	Mean	Standard deviation	Median	5th percentile	95th percentile
Width (m)	Glaciated	100	4260	2010	3630	2030	8290
	Fluvial	100	2290	1060	2020	972	4590
	Greenland	5335	3810	2080	3340	1410	7890
V-index	Glaciated	100	0.209	0.113	0.222	0.002	0.380
	Fluvial	100	0.019	0.091	0.007	-0.106	0.183
	Greenland	5335	0.239	0.137	0.233	0.022	0.471
C ratio	Glaciated	100	0.394	0.184	0.436	0.028	0.599
	Fluvial	100	0.014	0.295	0.021	-0.609	0.493
	Greenland	5335	0.436	0.265	0.469	-0.015	0.780

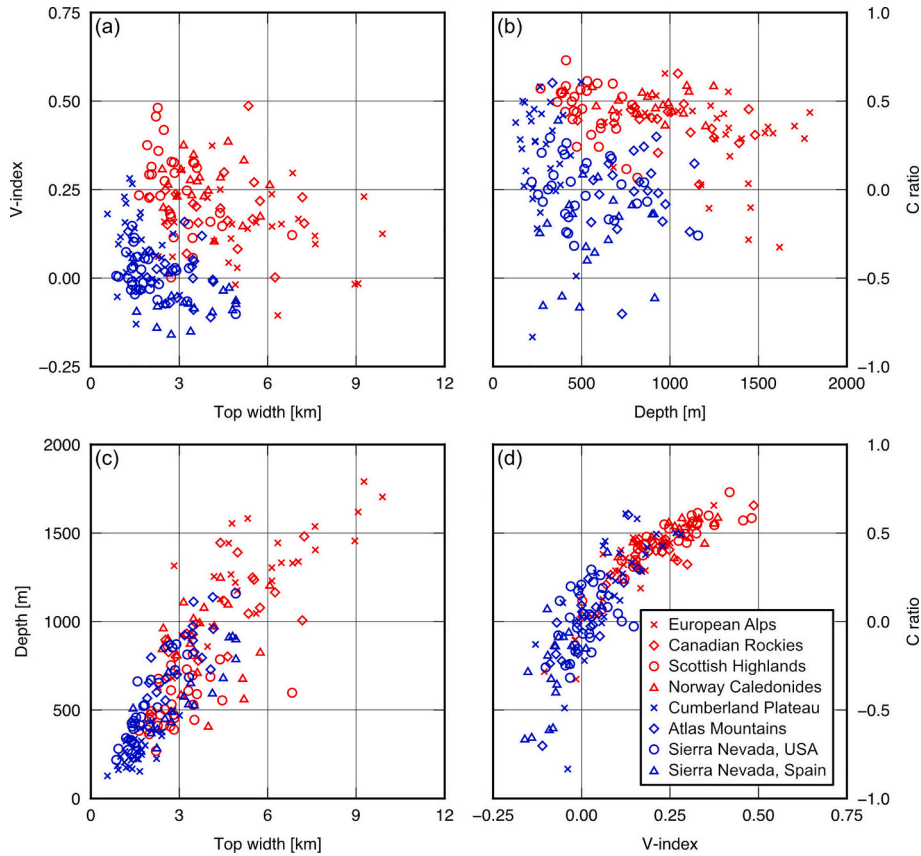
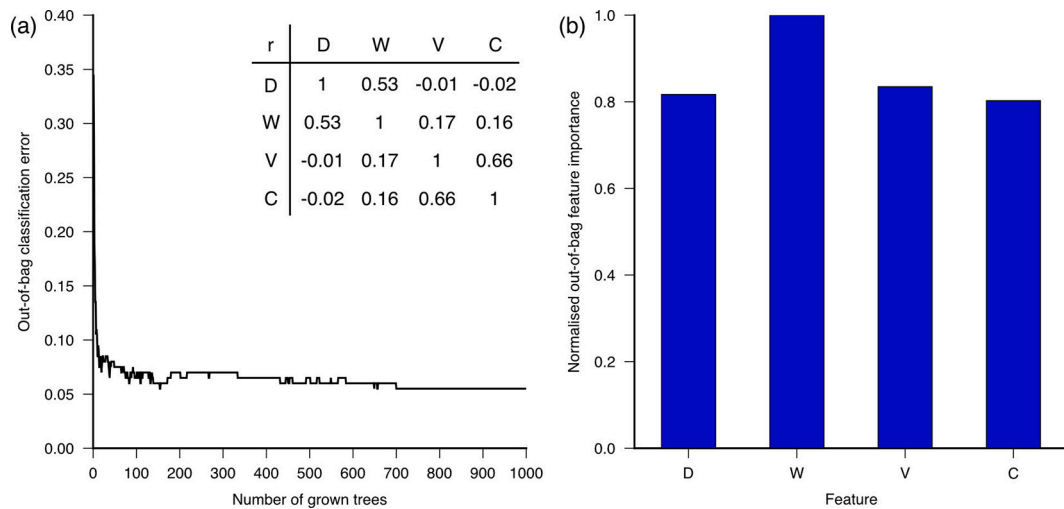
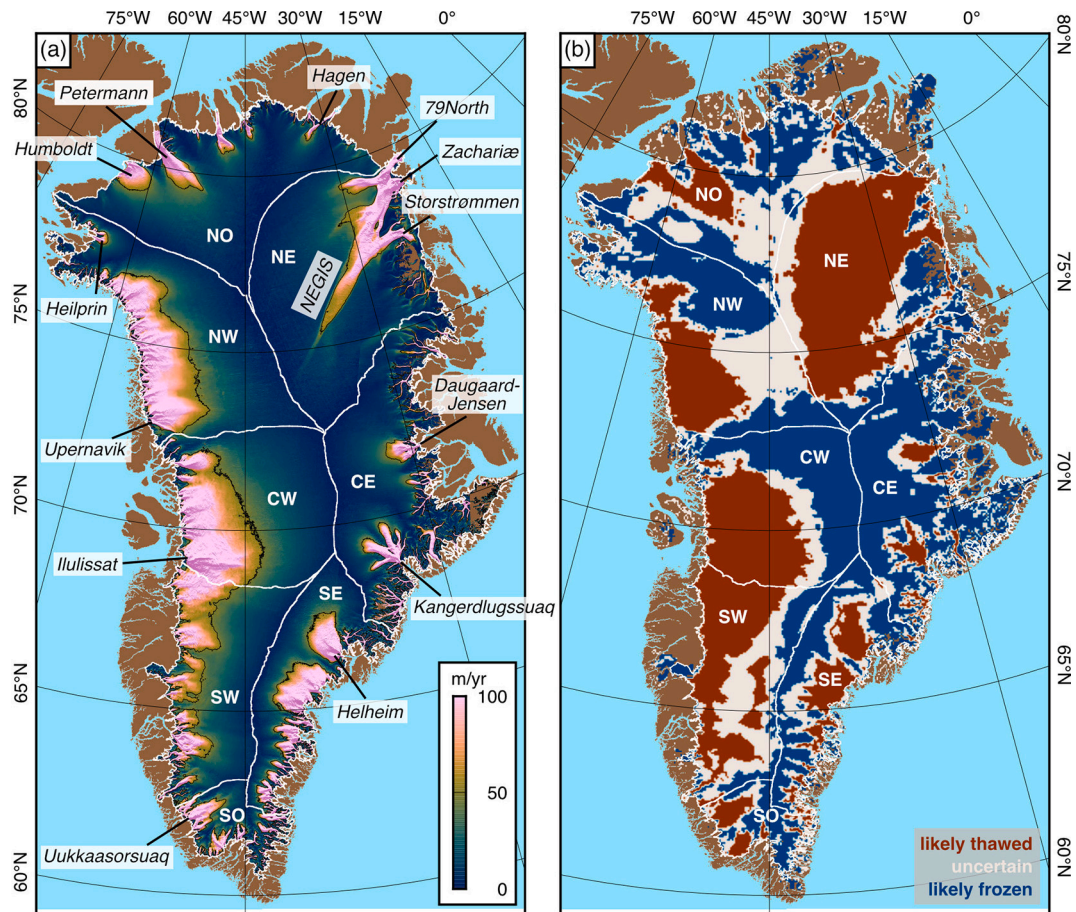


Fig. A1. Relationships between valley morphometric indices. (a) Valley top width vs. V-index. (b) Valley depth vs. C ratio. (c) Valley top width vs. depth. (d) V-index vs. C ratio. In panels a and b, the independent variables are poorly correlated, with a well-defined separation between glacial (red) and fluvial (blue) valleys in this feature space. In panels c and d, the independent variables are more strongly correlated; a greater degree of overlap is also apparent, although separation between glacial and fluvial valleys is still evident. This correlation is to be expected given that the two variables defining valley scale are plotted in panel c, and the two variables defining valley shape are plotted in panel d.



**Fig. A2.** Performance of the random forest classification scheme. (a) Out-of-bag (OOB) classification error for the random forest. The OOB error is the proportion of training samples that are misclassified having not been selected during the bootstrap aggregation process. The OOB error rate falls steeply as the number of decision trees in the random forest increases, and then levels off at  $\sim 0.06$  after approximately 200 trees, representing an OOB classification accuracy of 94 %. Inset shows the intercorrelation matrix between the four valley morphometrics used for classification. (b) Normalised feature importance based on the relative influence each of the four valley morphometrics has on the OOB classification error when included in (or removed from) the random forest algorithm.



**Fig. A3.** Greenland ice sheet dynamics. (a) Ice surface velocity (Joughin et al., 2018). The 50 m/yr contour, an approximate threshold of the onset of fast flow, is marked by the black outline. Selected outlet glaciers are labeled. (b) Synthesis of the likely basal thermal state of the ice sheet (MacGregor et al., 2022). White lines delineate major ice sheet drainage catchments (Zwally et al., 2012).

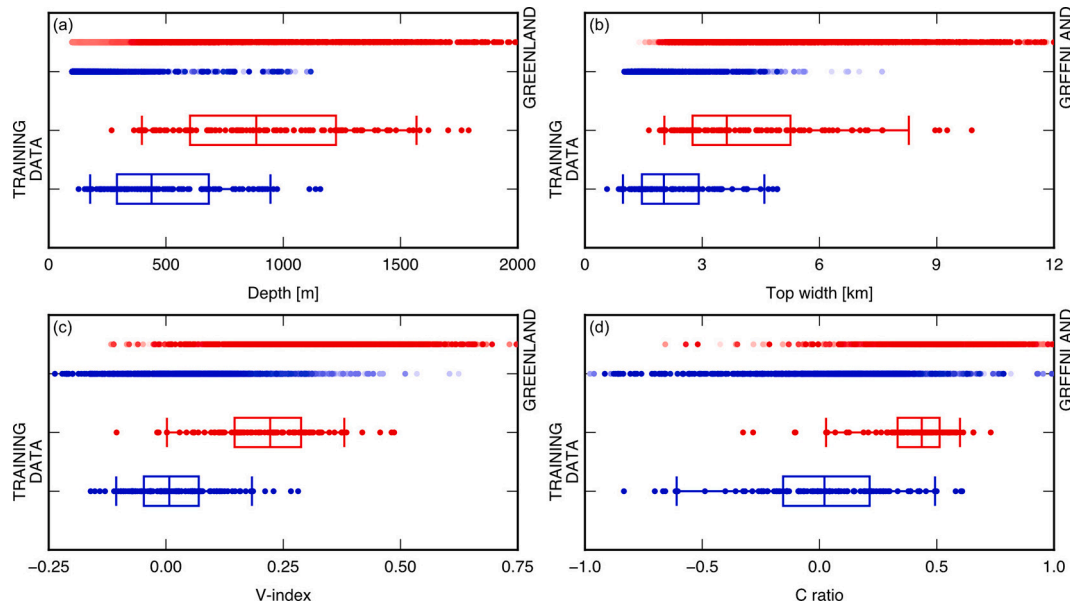


**Fig. A4.** Comparison of valley morphometrics in the training data and in Greenland. (a) Valley depth, (b) Valley top width, (c) V-index (V), (d) C ratio. Training data: filled circles represent valleys from fluvial (blue) or glacial (red) settings; boxplot marks the median, interquartile range, and 5th and 95th percentiles. Greenland data: filled circles represent valleys classified as 'fluvial' or 'glacial'; solidity of the colour represents valley score (see Fig. 8).

## References

- Alley, R.B., Andrews, J.T., Brigham-Grette, J., Clarke, G.K.C., Cuffey, K.M., Fitzpatrick, J. J., Funder, S., Marshall, S.J., Miller, G.H., Mitrovica, J.X., Muhs, D.R., Otto-Bliesner, B.L., Polyak, L., White, J.W.C., 2010. History of the Greenland Ice Sheet: paleoclimatic insights. *Quat. Sci. Rev.* 29, 1728–1756. <https://doi.org/10.1016/j.quascirev.2010.02.007>.
- Alley, R.B., Cuffey, K.M., Zoet, L.K., 2019. Glacial erosion: status and outlook. *Ann. Glaciol.* 60, 1–13. <https://doi.org/10.1017/aog.2019.38>.
- Allred, K.J., Luo, W., 2016. Quantifying and predicting the glacial extent using valley morphometry and data-mining techniques. *Ann. GIS* 22, 203–214. <https://doi.org/10.1080/19475683.2016.1195873>.
- Alwosheel, A., van Cranenburgh, S., Chorus, C.G., 2018. Is your dataset big enough? Sample size requirements when using artificial neural networks for discrete choice analysis. *J. Choice Model.* 28, 167–182. <https://doi.org/10.1016/j.jocm.2018.07.002>.
- Andrews, L.C., Catania, G.A., Hoffman, M.J., Gulley, J.D., Lüthi, M.P., Ryser, C., Hawley, R.L., Neumann, T.A., 2015. Direct observations of evolving subglacial drainage beneath the Greenland Ice Sheet. *Nature* 514, 80–83. <https://doi.org/10.1038/nature13796>.
- Aschwanden, A., Brinkerhoff, D.J., 2022. Calibrated mass loss projections from the Greenland Ice Sheet. *Geophys. Res. Lett.* 1–15. <https://doi.org/10.18739/A2G73752>.
- Bamber, J.L., Siegert, M.J., Griggs, J.A., Marshall, S.J., Spada, G., 2013. Paleofluvial mega-canyon beneath the central Greenland ice sheet. *Science* (80-. ) 341, 997–999. <https://doi.org/10.1126/science.1239794>.
- Baroni, C., Noti, V., Ciccacci, S., Righini, G., Salvatore, M.C., 2005. Fluvial origin of the valley system in northern Victoria Land (Antarctica) from quantitative geomorphic analysis. *Geol. Soc. Am. Bull.* 117, 212–228. <https://doi.org/10.1130/B25529.1>.
- Bartlett, O.T., Palmer, S.J., Schroeder, D.M., Mackie, E.J., Barrows, T.T., Graham, A.G.C., 2020. Geospatial simulations of airborne ice-penetrating radar surveying reveal elevation under-measurement bias for ice-sheet bed topography. *Ann. Glaciol.* 61, 46–57. <https://doi.org/10.1017/aog.2020.35>.
- Beaud, F., Venditti, J.G., Flowers, G.E., Koppes, M., 2018. Excavation of subglacial bedrock channels by seasonal meltwater flow. *Earth Surf. Process. Landf.* 43, 1960–1972. <https://doi.org/10.1002/esp.4367>.
- Bickerdike, H.L., Evans, D.J.A., Stokes, C.R., Ó Cofaigh, C., 2018. The glacial geomorphology of the Loch Lomond (Younger Dryas) Stadial in Britain: a review. *J. Quat. Sci.* 33, 1–54. <https://doi.org/10.1002/jqs.3010>.
- Bierman, P.R., Corbett, L.B., Graly, J.A., Neumann, T.A., Lini, A., Crosby, B.T., Rood, D. H., 2014. Preservation of a preglacial landscape under the center of the Greenland Ice Sheet. *Science* (80-. ) 344, 402–405. <https://doi.org/10.1126/science.1249047>.
- Bierman, P.R., Shakun, J.D., Corbett, L.B., Zimmerman, S.R., Rood, D.H., 2016. A persistent and dynamic East Greenland Ice Sheet over the past 7.5 million years. *Nature* 540, 256–260. <https://doi.org/10.1038/nature20147>.
- Boulton, G.S., Clark, C.D., 1990. A highly mobile Laurentide ice sheet revealed by satellite images of glacial lineations. *Nature* 346, 813–817. <https://doi.org/10.1038/346813a0>.
- Breiman, L., 2001. Random forests. *Mach. Learn.* 45, 5–32. <https://doi.org/10.1023/A:1010933404324>.
- Brigham, C.A.P., Crider, J.G., 2022. A new metric for morphologic variability using landform shape classification via supervised machine learning. *Geomorphology* 399, 108065. <https://doi.org/10.1016/j.geomorph.2021.108065>.
- Brook, M.S., Kirkbride, M.P., Brock, B.W., 2006. Quantified time scale for glacial valley cross-profile evolution in alpine mountains. *Geology* 34, 637–640. <https://doi.org/10.1130/G22700.1>.
- Bull, W.B., McFadden, L.D., 1977. Tectonic geomorphology north and south of the Garlock fault, California. In: Doehring, D.O. (Ed.), *Geomorphology in Arid Regions*. Routledge, pp. 115–138. <https://doi.org/10.4324/9780429299230>.
- Cazenave, A., Meyssignac, B., Ablain, M., Balmaseda, M., Bamber, J., Barletta, V., Beckley, B., Benveniste, J., Berthier, E., Blazquez, A., Boyer, T., Caceres, D., Chambers, D., Champollion, N., Chao, B., Chen, J., Cheng, L., Church, J.A., Chuter, S., Cogley, J.G., Dangendorf, S., Desbruyères, D., Döll, P., Domingues, C., Falk, U., Famiglietti, J., Fenoglio-Marc, L., Forsberg, R., Galassi, G., Gardner, A., Groh, A., Hamlington, B., Hogg, A., Horwath, M., Humphrey, V., Husson, L., Ishii, M., Jaeggi, A., Jevrejeva, S., Johnson, G., Kolodziejczyk, N., Kusche, J., Lambeck, K., Landerer, F., Leclercq, P., Legresy, B., Leuliette, E., Llovel, W., Longuevergne, L., Loomis, B.D., Luthcke, S.B., Marcos, M., Marzeion, B., Merchant, C., Merrifield, M., Milne, G., Mitchum, G., Mohajerani, Y., Monier, M., Monselesan, D., Nerem, S., Palanisamy, H., Paul, F., Perez, B., Piecuch, C.G., Ponte, R.M., Purkey, S.G., Reager, J.T., Rietbroek, R., Rignot, E., Riva, R., Roemmich, D.H., Sørensen, L.S., Sasgen, I., Schrama, E.J.O., Seneviratne, S.I., Shum, C.K., Spada, G., Stammer, D., van de Wal, R., Velicogna, I., von Schuckmann, K., Wada, Y., Wang, Y., Watson, C., Wiese, D., Wijffels, S., Westaway, R., Woppelmann, G., Wouters, B., 2018. Global sea-level budget 1993–present. *Earth Syst. Sci. Data* 10, 1551–1590. <https://doi.org/10.5194/essd-10-1551-2018>.
- Chambers, C., Greve, R., Altena, B., Lefevre, P.M., 2020. Possible impacts of a 1000 km long hypothetical subglacial river valley towards Petermann Glacier in northern Greenland. *Cryosph.* 14, 3747–3759. <https://doi.org/10.5194/tc-14-3747-2020>.
- Chandler, B.M.P., Lovell, H., Boston, C.M., Lukas, S., Barr, I.D., Benediktsson, Í.Ö., Benn, D.I., Clark, C.D., Darvill, C.M., Evans, D.J.A., Ewertowski, M.W., Loibl, D., Margold, M., Otto, J.C., Roberts, D.H., Stokes, C.R., Storrar, R.D., Stroeven, A.P., 2018. Glacial geomorphological mapping: a review of approaches and frameworks for best practice. *Earth-Sci. Rev.* 185, 806–846. <https://doi.org/10.1016/j.earscirev.2018.07.015>.
- Clark, C.D., Ely, J.C., Hindmarsh, R.C.A., Bradley, S., Ignézi, A., Fabel, D., Ó Cofaigh, C., Chiverrell, R.C., Scourse, J., Benetti, S., Bradwell, T., Evans, D.J.A., Roberts, D.H., Burke, M., Callard, S.L., Medialdea, A., Saher, M., Small, D., Smedley, R.K., Gasson, E., Gregoire, L., Gandy, N., Hughes, A.L.C., Ballantyne, C., Bateman, M.D., Bigg, G.R., Doole, J., Dove, D., Duller, G.A.T., Jenkins, G.T.H., Livingstone, S.L., McCarron, S., Moreton, S., Pollard, D., Praeg, D., Sejrup, H.P., Van Landeghem, K.J. J., Wilson, P., 2022. Growth and retreat of the last British–Irish Ice Sheet, 31000 to 15000 years ago: the BRITICE-CHRONO reconstruction. *Boreas*. <https://doi.org/10.1111/bor.12594>.
- Cook, S.J., Swift, D.A., Kirkbride, M.P., Knight, P.G., Waller, R.I., 2020. The empirical basis for modelling glacial erosion rates. *Nat. Commun.* 11, 759. <https://doi.org/10.1038/s41467-020-14583-8>.

- Cooper, M.A., Michaelides, K., Siegert, M.J., Bamber, J.L., 2016. Paleofluvial landscape inheritance for Jakobshavn Isbræ catchment, Greenland. *Geophys. Res. Lett.* 43, 6350–6357. <https://doi.org/10.1002/2016GL069458>.
- Cooper, M.A., Jordan, T.M., Schroeder, D.M., Siegert, M.J., Williams, C.N., Bamber, J.L., 2019. Subglacial roughness of the Greenland Ice Sheet: relationship with contemporary ice velocity and geology. *Cryosph.* 13, 3093–3115. <https://doi.org/10.5194/tc-13-3093-2019>.
- Cowton, T., Nienow, P., Bartholomew, I., Sole, A., Mair, D., 2012. Rapid erosion beneath the Greenland ice sheet. *Geology* 40, 343–346. <https://doi.org/10.1130/G32687.1>.
- Dam, G., Sønderholm, M., Sørensen, E.V., 2020. Inherited basement canyons: Impact on sediment distribution in the North Atlantic. *Terra Nova* 32, 272–280. <https://doi.org/10.1111/ter.12459>.
- Davila, A.F., Fairén, A.G., Stokes, C.R., Platz, T., Rodriguez, A.P., Lacelle, D., Dohm, J., Pollard, W., 2013. Evidence for Hesperian glaciation along the Martian dichotomy boundary. *Geology* 41, 755–758. <https://doi.org/10.1130/G34201.1>.
- DeConto, R.M., Pollard, D., Wilson, P.A., Pälike, H., Lear, C.H., Pagani, M., 2008. Thresholds for Cenozoic bipolar glaciation. *Nature* 455, 652–656. <https://doi.org/10.1038/nature07337>.
- Dolan, A.M., Hunter, S.J., Hill, D.J., Haywood, A.M., Koenig, S.J., Otto-Bliesner, B.L., Abe-Ouchi, A., Bragg, F., Chan, W.L., Chandler, M.A., Contoux, C., Jost, A., Kamae, Y., Lohmann, G., Lunt, D.J., Ramstein, G., Rosenbloom, N.A., Sohl, L., Stepanek, C., Ueda, H., Yan, Q., Zhang, X., 2015. Using results from the PlioMIP ensemble to investigate the Greenland Ice Sheet during the mid-Pliocene Warm Period. *Clim. Past* 11, 403–424. <https://doi.org/10.5194/cp-11-403-2015>.
- Edwards, T.L., Brandon, M.A., Durand, G., Edwards, N.R., Gollledge, N.R., Holden, P.B., Nias, L.J., Payne, A.J., Ritz, C., Wernecke, A., 2019. Revisiting Antarctic ice loss due to marine ice-cliff instability. *Nature* 566, 58–64. <https://doi.org/10.1038/s41586-019-0901-4>.
- Edwards, T.L., Nowicki, S., Marzeion, B., Hock, R., Goelzer, H., Seroussi, H., Jourdain, N.C., Slater, D.A., Turner, F.E., Smith, C.H., McKenna, C.M., Simon, E., Abe-Ouchi, A., Gregory, J.M., Larour, E., Lipscomb, W.H., Payne, A.J., Shepherd, A., Agosta, C., Alexander, P., Albrecht, T., Anderson, B., Asay-Davis, X., Aschwanden, A., Barthel, A., Bliss, A., Calov, R., Chambers, C., Champollion, N., Choi, Y., Cullather, R., Cuzzone, J., Dumas, C., Felikson, D., Fettweis, X., Fujita, K., Galton-Fenzi, B.K., Gladstone, R., Gollledge, N.R., Greve, R., Hattermann, T., Hoffman, M.J., Humbert, A., Huss, M., Huybrechts, P., Immerzeel, W., Kleiner, T., Kraaijenbrink, P., Le Clec'h, S., Lee, V., Leguy, G., Little, C.M., Lowry, D.P., Mallet, J.-H., Martin, D.F., Maussion, F., Morlighem, M., O'Neill, J.F., Nias, I., Pattyn, F., Pelle, T., Price, S.F., Quiquet, A., Radić, V., Reese, R., Rounce, D.R., Rückamp, M., Sakai, A., Shafer, C., Schlegel, N.-J., Shannon, S., Smith, R.S., Straneo, F., Sun, S., Tarasov, L., Trusel, L.D., Van Breedam, J., van de Wal, R., van den Broeke, M., Winkelmann, R., Zekollari, H., Zhao, C., Zhang, T., Zwinger, T., 2021. Projected land ice contributions to twenty-first-century sea level rise. *Nature* 593, 74–82. <https://doi.org/10.1038/s41586-021-03302-y>.
- Egholm, D.L., Nielsen, S.B., Pedersen, V.K., Lesemann, J.-E., 2009. Glacial effects limiting mountain height. *Nature* 460, 884–887. <https://doi.org/10.1038/nature08263>.
- Eldred, J.S., Harding, I.C., Wilson, P.A., Butler, E., Roberts, A.P., 2007. Continental ice in Greenland during the Eocene and Oligocene. *Nature* 446, 176–179. <https://doi.org/10.1038/nature05591>.
- Elmes, A., Alemohammad, H., Avery, R., Caylor, K., Eastman, J.R., Fishgold, L., Friedl, M.A., Jain, M., Kohli, D., Bayas, J.C.L., Lunga, D., McCarty, J.L., Pontius, R. G., Reinmann, A.B., Rogan, J., Song, L., Stoyanova, H., Ye, S., Yi, Z.F., Estes, L., 2020. Accounting for training data error in machine learning applied to earth observations. *Remote Sens.* 12, 1–39. <https://doi.org/10.3390/rs12061034>.
- European Space Agency, 2021. Copernicus Global Digital Elevation Model. Distributed by OpenTopography [WWW Document]. doi:<https://doi.org/10.5069/G9028PQB>.
- Flesche Kleiven, H., Jansen, E., Fronval, T., Smith, T.M., 2002. Intensification of Northern Hemisphere glaciations in the circum Atlantic region (3.5–2.4 Ma) - ice-rafted detritus evidence. *Palaeogeogr. Palaeoclimatol. Palaeoecol.* 184, 213–223. [https://doi.org/10.1016/S0031-0182\(01\)00407-2](https://doi.org/10.1016/S0031-0182(01)00407-2).
- Franke, S., Jansen, D., Binder, T., Dörr, N., Helm, V., Paden, J., Steinhage, D., Eisen, O., 2020. Bed topography and subglacial landforms in the onset region of the Northeast Greenland Ice Stream. *Ann. Glaciol.* 61, 143–153. <https://doi.org/10.1017/aog.2020.12>.
- Franke, S., Eisermann, H., Jokat, W., Eagles, G., Asseng, J., Miller, H., Steinhage, D., Helm, V., Eisen, O., Jansen, D., 2021. Preserved landscapes underneath the Antarctic Ice Sheet reveal the geomorphological history of Jutulstraumen Basin. *Earth Surf. Process. Landf.* 46, 2728–2745. <https://doi.org/10.1002/esp.5203>.
- Franke, S., Bons, P.D., Westhoff, J., Weikusat, I., Binder, T., Streng, K., Steinhage, D., Helm, V., Eisen, O., Paden, J.D., Eagles, G., Jansen, D., 2022a. Holocene ice-stream shutdown and drainage basin reconfiguration in northeast Greenland. *Nat. Geosci.* 15, 995–1001. <https://doi.org/10.1038/s41561-022-01082-2>.
- Franke, S., Jansen, D., Binder, T., Paden, J.D., Dörr, N., Gerber, T.A., Miller, H., Dahl-Jensen, D., Helm, V., Steinhage, D., Weikusat, I., Wilhelms, F., Eisen, O., 2022b. Airborne ultra-wideband radar sounding over the shear margins and along flow lines at the onset region of the Northeast Greenland Ice Stream. *Earth Syst. Sci. Data* 14, 763–779. <https://doi.org/10.5194/essd-14-763-2022>.
- Gillespie, A.R., Clark, D.H., 2011. Glaciations of the Sierra Nevada, California, USA. *Dev. Quat. Sci.* 447–462. <https://doi.org/10.1016/B978-0-444-53447-7.00034-9>.
- Goelzer, H., Nowicki, S., Payne, A., Larour, E., Seroussi, H., Lipscomb, W.H., Gregory, J., Abe-Ouchi, A., Shepherd, A., Simon, E., Agosta, C., Alexander, P., Aschwanden, A., Barthel, A., Calov, R., Chambers, C., Choi, Y., Cuzzone, J., Dumas, C., Edwards, T., Felikson, D., Fettweis, X., Gollledge, N.R., Greve, R., Humbert, A., Huybrechts, P., Le Clec'h, S., Lee, V., Leguy, G., Little, C., Lowry, D., Morlighem, M., Nias, I., Quiquet, A., Rückamp, M., Schlegel, N.J., Slater, D.A., Smith, R., Straneo, F., Tarasov, L., Van De Wal, R., Van Den Broeke, M., 2020. The future sea-level contribution of the Greenland ice sheet: a multi-model ensemble study of ISMIP6. *Cryosph.* 14, 3071–3096. <https://doi.org/10.5194/tc-14-3071-2020>.
- Gogineni, S., Tammana, D., Braaten, D., Leuschen, C., Akins, T., Legarsky, J., Kanagaratnam, P., Stiles, J., Allen, C., Jezek, K., 2001. Coherent radar ice thickness measurements over the Greenland ice sheet. *J. Geophys. Res. Atmos.* 106, 33761–33772. <https://doi.org/10.1029/2001JD900183>.
- Grau Galofre, A., Jellinek, A.M., 2017. The geometry and complexity of spatial patterns of terrestrial channel networks: Distinctive fingerprints of erosional regimes. *J. Geophys. Res. Earth Surf.* 122, 1037–1059. <https://doi.org/10.1002/2016JF003825>.
- Grömping, U., 2009. Variable importance assessment in regression: Linear regression versus random forest. *Am. Stat.* 63, 308–319. <https://doi.org/10.1198/tast.2009.08199>.
- Hall, A.M., Ebert, K., Kleman, J., Nesje, A., Ottesen, D., 2013. Selective glacial erosion on the Norwegian passive margin. *Geology* 41, 1203–1206. <https://doi.org/10.1130/G34806.1>.
- Harbor, J.M., Wheeler, D.A., 1992. On the mathematical description of glaciated valley cross sections. *Earth Surf. Process. Landf.* 17, 477–485. <https://doi.org/10.1002/esp.3290170507>.
- Haywood, A.M., Valdes, P.J., Aze, T., Barlow, N., Burke, A., Dolan, A.M., von der Heydt, A.S., Hill, D.J., Jamieson, S.S.R., Otto-Bliesner, B.L., Salzmann, U., Saupe, E., Voss, J., 2019. What can Palaeoclimate Modelling do for you? *Earth Syst. Environ.* 3, 1–18. <https://doi.org/10.1007/s41748-019-00093-1>.
- Henriksen, N., Higgins, A.K., Kalsbeek, F., Pulvertaft, T.C.R., 2009. Greenland from Archaean to Quaternary: Descriptive Text to the 1995 Geological Map of Greenland, 1:2500000, 2nd edition vol 18. *Geol. Surv. Denmark Greenl. Bull.*, p. 126.
- Hillel, G.E., Baden, C.W., Dobbs, S.C., Plante, Z., Sare, R., Steelquist, A.T., 2020. A curvature-based method for measuring valley width applied to glacial and fluvial landscapes. *J. Geophys. Res. Earth Surf.* 125, 1–16. <https://doi.org/10.1029/2020JF005605>.
- Howat, I.M., Negrete, A., Smith, B.E., 2014. The Greenland Ice Mapping Project (GIMP) land classification and surface elevation data sets. *Cryosph.* 8, 1509–1518. <https://doi.org/10.5194/tc-8-1509-2014>.
- Howat, I.M., Negrete, A., Smith, B.E., 2022. MEASURES Greenland Ice Mapping Project (GIMP) Digital Elevation Model from GeoEye and WorldView Imagery, Version 2 [WWW Document]. NASA Natl. Snow Ice Data Cent. Distrib. Act. Arch. Cent. <https://doi.org/10.5067/BHS455GAMFVY>.
- Jamieson, S.S.R., Hulton, N.R.J., Hagdorn, M., 2008. Modelling landscape evolution under ice sheets. *Geomorphology* 97, 91–108. <https://doi.org/10.1016/j.geomorph.2007.02.047>.
- Jamieson, S.S.R., Stokes, C.R., Ross, N., Rippin, D.M., Bingham, R.G., Wilson, D.S., Margold, M., Bentley, M.J., 2014. The glacial geomorphology of the Antarctic ice sheet bed. *Antarct. Sci.* 26, 724–741. <https://doi.org/10.1017/S09541020140000212>.
- Jansen, E., Fronval, T., Rack, F., Channell, J.E.T., 2000. Pliocene-Pleistocene ice rafting history and cyclicity in the Nordic Seas during the last 3.5 Myr. *Paleoceanography* 15, 709–721. <https://doi.org/10.1029/1999PA000435>.
- Jess, S., Peace, A.L., Schiffer, C., 2020. Sediment supply on the West Greenland passive margin: redirection of a large pre-glacial drainage system. *J. Geol. Soc. Lond.* 177, 1149–1160. <https://doi.org/10.1144/jgs2020-028>.
- Joughin, I., Smith, B.E., Howat, I.M., 2018. A complete map of Greenland ice velocity derived from satellite data collected over 20 years. *J. Glaciol.* 64, 1–11. <https://doi.org/10.1017/jog.2017.73>.
- Kirkham, J.D., Hogan, K.A., Larter, R.D., Arnold, N.S., Ely, J.C., Clark, C.D., Self, E., Games, K., Huuse, M., Stewart, M.A., Ottesen, D., Dowdeswell, J.A., 2022. Tunnel valley formation beneath deglaciating mid-latitude ice sheets: observations and modelling. *Quat. Sci. Rev.* 107680. <https://doi.org/10.1016/j.quascirev.2022.107680>.
- Kleman, J., Hattestrand, C., Borgstrom, I., Stroeve, A., 1997. Fennoscandian palaeoglaciation reconstructed using a glacial geological inversion model. *J. Glaciol.* 43, 283–299. <https://doi.org/10.1017/S0022143000003233>.
- Koenig, S.J., Dolan, A.M., De Boer, B., Stone, E.J., Hill, D.J., Deconto, R.M., Abe-Ouchi, A., Lunt, D.J., Pollard, D., Quiquet, A., Saito, F., Savage, J., Van De Wal, R., 2015. Ice sheet model dependency of the simulated Greenland Ice Sheet in the mid-Pliocene. *Clim. Past* 11, 369–381. <https://doi.org/10.5194/cp-11-369-2015>.
- Lelandais, T., Mourgues, R., Ravier, É., Pochat, S., Strzeczynski, P., Bourgeois, O., 2016. Experimental modeling of pressurized subglacial water flow: Implications for tunnel valley formation. *J. Geophys. Res. Earth Surf.* 121, 2022–2041. <https://doi.org/10.1002/2016JF003957>.
- Li, L., Aitken, A.R.A., Lindsay, M.D., Kulassa, B., 2022. Sedimentary basins reduce stability of Antarctic ice streams through groundwater feedbacks. *Nat. Geosci.* 15, 645–650. <https://doi.org/10.1038/s41561-022-00992-5>.
- Livingstone, S.J., Chu, W., Ely, J.C., Kingslake, J., 2017. Paleofluvial and subglacial channel networks beneath Humboldt Glacier, Greenland. *Geology* 45, 551–554. <https://doi.org/10.1130/G38860.1>.
- MacGregor, J.A., Bottke, W.F., Fahnestock, M.A., Harbeck, J.P., Kjær, K.H., Paden, J.D., Stillman, D.E., Stüding, M., 2019. A possible second large subglacial impact crater in northwest Greenland. *Geophys. Res. Lett.* 46, 1496–1504. <https://doi.org/10.1029/2018GL078126>.
- MacGregor, J.A., Boisvert, L.N., Medley, B., Petty, A.A., Harbeck, J.P., Bell, R.E., Blair, J. B., Blanchard-Wrigglesworth, E., Buckley, E.M., Christoffersen, M.S., Cochran, J.R., Csathó, B.M., De Marco, E.L., Dominguez, R.T., Fahnestock, M.A., Farrell, S.L., Gogineni, S.P., Greenbaum, J.S., Hansen, C.M., Hofton, M.A., Holt, J.W., Jezek, K.C., Koenig, L.S., Kurtz, N.T., Kwok, R., Larsen, C.F., Leuschen, C.J., Locke, C.D., Manizade, S.S., Martin, S., Neumann, T.A., Nowicki, S.M.J., Paden, J.D., Richter-Menge, J.A., Rignot, E.J., Rodríguez-Morales, F., Siegfried, M.R., Smith, B.E.,

- Sonntag, J.G., Studinger, M., Tinto, K.J., Truffer, M., Wagner, T.P., Woods, J.E., Young, D.A., Yungel, J.K., 2021. The scientific legacy of NASA's Operation IceBridge. *Rev. Geophys.* 59, 1–65. <https://doi.org/10.1029/2020RG000712>.
- MacGregor, J.A., Chu, W., Colgan, W.T., Fahnestock, M.A., Felikson, D., Karlsson, N.B., Nowicki, S.M.J., Studinger, M., 2022. GBaTSv2: a revised synthesis of the likely basal thermal state of the Greenland Ice Sheet. *Cryosph.* 16, 3033–3049. <https://doi.org/10.5194/tc-16-3033-2022>.
- Margold, M., Jansson, K.N., Kleman, J., Stroeven, A.P., Clague, J.J., 2013. Retreat pattern of the Cordilleran Ice Sheet in central British Columbia at the end of the last glaciation reconstructed from glacial meltwater landforms. *Boreas* 42, 830–847. <https://doi.org/10.1111/bor.12007>.
- Miller, K.G., Browning, J.V., Schmelz, W.J., Kopp, R.E., Mountain, G.S., Wright, J.D., 2020. Cenozoic sea-level and cryospheric evolution from deep-sea geochemical and continental margin records. *Sci. Adv.* 6.
- Morlighem, M., Williams, C.N., Rignot, E., An, L., Arndt, J.E., Bamber, J.L., Catania, G., Chauché, N., Dowdeswell, J.A., Dorschel, B., Fenty, I., Hogan, K., Howat, I., Hubbard, A., Jakobsson, M., Jordan, T.M., Kjeldsen, K.K., Millan, R., Mayer, L., Mouginot, J., Noël, B.P.Y., O'Coiffaigh, C., Palmer, S., Rysgaard, S., Seroussi, H., Siegert, M.J., Slabon, P., Straneo, F., van den Broeke, M.R., Weinrebe, W., Wood, M., Zinglensen, K.B., 2017. BedMachine v3: complete bed topography and ocean bathymetry mapping of Greenland from multibeam echo sounding combined with mass conservation. *Geophys. Res. Lett.* 44, 11,051–11,061. <https://doi.org/10.1002/2017GL074954>.
- Mudelsee, M., Raymo, M.E., 2005. Slow dynamics of the Northern Hemisphere glaciation. *Paleoceanography* 20. <https://doi.org/10.1029/2005PA001153>.
- Noble, T.L., Rohling, E.J., Aitken, A.R.A., Bostock, H.C., Chase, Z., Gomez, N., Jong, L.M., King, M.A., Mackintosh, A.N., McCormack, F.S., McKay, R.M., Menviel, L., Phipps, S. J., Weber, M.E., Fogwill, C.J., Gayen, B., Gollidge, N.R., Gwyther, D.E., Hogg, A.M. C., Martos, Y.M., Pena-Molino, B., Roberts, J., Flierdt, T., Williams, T., 2020. The sensitivity of the Antarctic Ice Sheet to a changing climate: past, present and future. *Rev. Geophys.* 1–89 <https://doi.org/10.1029/2019rg000663>.
- Paden, J., Li, J., Leuschen, C., Rodriguez-Morales, F., Hale, R., 2019. IceBridge MCoRDS L2 Ice Thickness, Version 1 [WWW Document]. NASA Natl. Snow Ice Data Cent. Distrib. Act. Arch. Cent, Boulder, Color, USA. <https://doi.org/10.5067/GDQ0CUCVTE2Q>.
- Pattyn, F., Van Huele, W., 1998. Power law or power flaw? *Earth Surf. Process. Landf.* 23, 761–767. [https://doi.org/10.1002/\(SICI\)1096-9837\(199808\)23:8<761::AID-ESP892>3.0.CO;2-K](https://doi.org/10.1002/(SICI)1096-9837(199808)23:8<761::AID-ESP892>3.0.CO;2-K).
- Paxman, G.J.G., Tinto, K.J., Austermann, J., 2021. Neogene–Quaternary uplift and landscape evolution in northern Greenland recorded by subglacial valley morphology. *J. Geophys. Res. Earth Surf.* 126, 1–24. <https://doi.org/10.1029/2021JF006395>.
- Paxman, G.J.G., Austermann, J., Hollyday, A., 2022. Total isostatic response to the complete unloading of the Greenland and Antarctic Ice Sheets. *Sci. Rep.* 12, 11399. <https://doi.org/10.1038/s41598-022-15440-y>.
- Penck, A., 1905. Glacial features in the surface of the alps. *J. Geol.* 13.
- Porter, S.C., 1989. Some geological implications of average Quaternary glacial conditions. *Quat. Res.* 32, 245–261. [https://doi.org/10.1016/0033-5894\(89\)90092-6](https://doi.org/10.1016/0033-5894(89)90092-6).
- Prasicek, G., Otto, J.C., Montgomery, D.R., Schrott, L., 2014. Multi-scale curvature for automated identification of glaciated mountain landscapes. *Geomorphology* 209, 53–65. <https://doi.org/10.1016/j.geomorph.2013.11.026>.
- Robb, C., Willis, I., Arnold, N., Gudmundsson, S., 2015. A semi-automated method for mapping glacial geomorphology tested at Breidamerkjökull, Iceland. *Remote Sens. Environ.* 163, 80–90. <https://doi.org/10.1016/j.rse.2015.03.007>.
- Rogers, C.M., Engelder, T., 2004. The feedback between joint-zone development and downward erosion of regularly spaced canyons in the Navajo Sandstone, Zion National Park, Utah. *Geol. Soc. Spec. Publ.* 231, 49–71. <https://doi.org/10.1144/GSL.SP.2004.231.01.04>.
- Rose, K.C., Ferraccioli, F., Jamieson, S.S.R., Bell, R.E., Corr, H., Creyts, T.T., Braaten, D., Jordan, T.A., Fretwell, P.T., Damaske, D., 2013. Early East Antarctic Ice Sheet growth recorded in the landscape of the Gamburtsev Subglacial Mountains. *Earth Planet. Sci. Lett.* 375, 1–12. <https://doi.org/10.1016/j.epsl.2013.03.053>.
- Schaefer, J.M., Finkel, R.C., Balco, G., Alley, R.B., Caffee, M.W., Briner, J.P., Young, N.E., Gow, A.J., Schwartz, R., 2016. Greenland was nearly ice-free for extended periods during the Pleistocene. *Nature* 540, 252–255. <https://doi.org/10.1038/nature20146>.
- Shreve, R.L., 1972. Movement of water in glaciers. *J. Glaciol.* 11, 205–214. <https://doi.org/10.1086/330839>.
- Solgaard, A.M., Reeh, N., Japsen, P., Nielsen, T., 2011. Snapshots of the Greenland ice sheet configuration in the Pliocene to early Pleistocene. *J. Glaciol.* 57, 871–880. <https://doi.org/10.3189/002214311798043816>.
- Stokes, M., Mather, A.E., Belfoul, A., Farik, F., 2008. Active and passive tectonic controls for transverse drainage and river gorge development in a collisional mountain belt (Dades Gorges, High Atlas Mountains, Morocco). *Geomorphology* 102, 2–20. <https://doi.org/10.1016/j.geomorph.2007.06.015>.
- Straneo, F., Heimbach, P., 2013. North Atlantic warming and the retreat of Greenland's outlet glaciers. *Nature* 504, 36–43. <https://doi.org/10.1038/nature12854>.
- Strunk, A., Knudsen, M.F., Egholm, D.L., Jansen, J.D., Levy, L.B., Jacobsen, B.H., Larsen, N.K., 2017. One million years of glaciation and denudation history in west Greenland. *Nat. Commun.* 8, 1–8. <https://doi.org/10.1038/ncomms14199>.
- Sugden, D.E., 1968. The selectivity of glacial erosion in the Cairngorm Mountains, Scotland. *Trans. Inst. Br. Geogr.* 45, 79. <https://doi.org/10.2307/621394>.
- Sugden, D.E., 1977. Reconstruction of the morphology, dynamics, and thermal characteristics of the laurentide ice sheet at its maximum. *Arct. Alp. Res.* 9, 21–47. <https://doi.org/10.1080/00040851.1977.12003898>.
- Sugden, D.E., John, B.S., 1976. *Glaciers and Landscape*. Edward Arnold, London.
- The Imbie Team, 2020. Mass balance of the Greenland Ice Sheet from 1992 to 2018. *Nature* 579, 233–239. <https://doi.org/10.1038/s41586-019-1855-2>.
- Tripati, A., Darby, D., 2018. Evidence for ephemeral middle Eocene to early Oligocene Greenland glacial ice and pan-Arctic sea ice. *Nat. Commun.* 9, 1–11. <https://doi.org/10.1038/s41467-018-03180-5>.
- van der Vegt, P., Janszen, A., Moscarriello, A., 2012. Tunnel valleys: current knowledge and future perspectives. *Geol. Soc. Spec. Publ.* 368, 75–97. <https://doi.org/10.1144/SP368.13>.
- Wessel, P., Luis, J.F., Uieda, L., Scharroo, R., Wobbe, F., Smith, W.H.F., Tian, D., 2019. The Generic Mapping Tools Version 6. *Geochem. Geophys. Geosyst.* 20, 5556–5564. <https://doi.org/10.1029/2019GC008515>.
- Whitehouse, P.L., Gomez, N., King, M.A., Wiens, D.A., 2019. Solid Earth change and the evolution of the Antarctic Ice Sheet. *Nat. Commun.* 10, 503. <https://doi.org/10.1038/s41467-018-08068-y>.
- Zimmer, P.D., Gabet, E.J., 2018. Assessing glacial modification of bedrock valleys using a novel approach. *Geomorphology* 318, 336–347. <https://doi.org/10.1016/j.geomorph.2018.06.021>.
- Zwally, H.J., Giovinetto, M.B., Beckley, M.A., Saba, J.L., 2012. Antarctic and Greenland Drainage Systems [WWW Document]. GSFC Cryospheric Sci. Lab. URL [http://icesa.t4.gsfc.nasa.gov/cryo\\_data/ant\\_grn\\_drainage\\_systems.php](http://icesa.t4.gsfc.nasa.gov/cryo_data/ant_grn_drainage_systems.php) (accessed 2.1.20).